

## Supplementary Information

### **Nile Blue Functionalized Graphene Aerogel as a Pseudocapacitive Negative Electrode Material Across the Full pH Range**

*Yasin Shabangoli<sup>a</sup>, Mohammad S. Rahmanifar<sup>b</sup>, Abolhassan Noori<sup>a</sup>, Maher F. El-Kady<sup>c</sup>, Richard B. Kaner<sup>\*c</sup> and Mir F. Mousavi<sup>\*a</sup>*

<sup>a</sup> Department of Chemistry, Faculty of Basic Sciences, Tarbiat Modares University, Tehran, 14115-175, Iran

<sup>b</sup> Faculty of Basic Sciences, Shahed University, Tehran 3319118-651, Iran

<sup>c</sup> Department of Chemistry and Biochemistry, Department of Materials Science and Engineering, and California NanoSystems Institute, University of California, Los Angeles (UCLA), CA 90095, USA

\* e-mail: *kaner@chem.ucla.edu; mousavim@modares.ac.ir*

## 1. Experimental Section

### 1.1. Fabrication of Electrodes/Devices

We fabricated NB-GA electrodes using stainless steel (SS, grade 316, 0.11 mm thick) with a geometric area of  $1.0 \text{ cm}^2$  as a current collector. SS pieces were cleaned by a 1:1 acetone-ethanol mixture for 10 minutes in a sonication bath prior to use, and then were washed thoroughly with DI water. For the preparation of the NB-GA electrodes, a mixture of the as-prepared active material powder, carbon black and polytetrafluoroethylene (PTFE) with a wt% ratio of 85:10:5 was pressed onto  $1.0 \text{ cm}^2$  SS and dried at  $60 \text{ }^\circ\text{C}$  for 2 h in air. The mass loading of the electrode active materials on each electrode was about  $2 \text{ mg cm}^{-2}$ .

For fabrication of the symmetric NB-GA || NB-GA device, we used cellulosic paper or Celgard M824 as a separator, and all the components were held together with lamination by pressing between two sheets. The NB-GA || NB-GA symmetric device was designed for operation in an acidic ( $1.0 \text{ M H}_2\text{SO}_4$ ) electrolyte. The NB-GA ||  $\text{MnO}_2$  and NB-GA || LDH asymmetric devices were fabricated for operation in neutral ( $1.0 \text{ M Na}_2\text{SO}_4$ ) and alkaline ( $1.0 \text{ M KOH}$ ) electrolytes, respectively. For approaching the maximum capacitance and operating voltage window, the mass ratio between the positive and negative electrodes ( $m^+/m^-$ ) of the NB-GA ||  $\text{MnO}_2$  and NB-GA || LDH asymmetric devices were optimized according to charge balance theory as 0.35 and 0.5, respectively.<sup>1</sup> Mass loadings of the Ni-Co-Fe LDH and  $\text{MnO}_2$  electrodes were  $1.0 \text{ mg cm}^{-2}$  and  $0.7 \text{ mg cm}^{-2}$ , respectively.

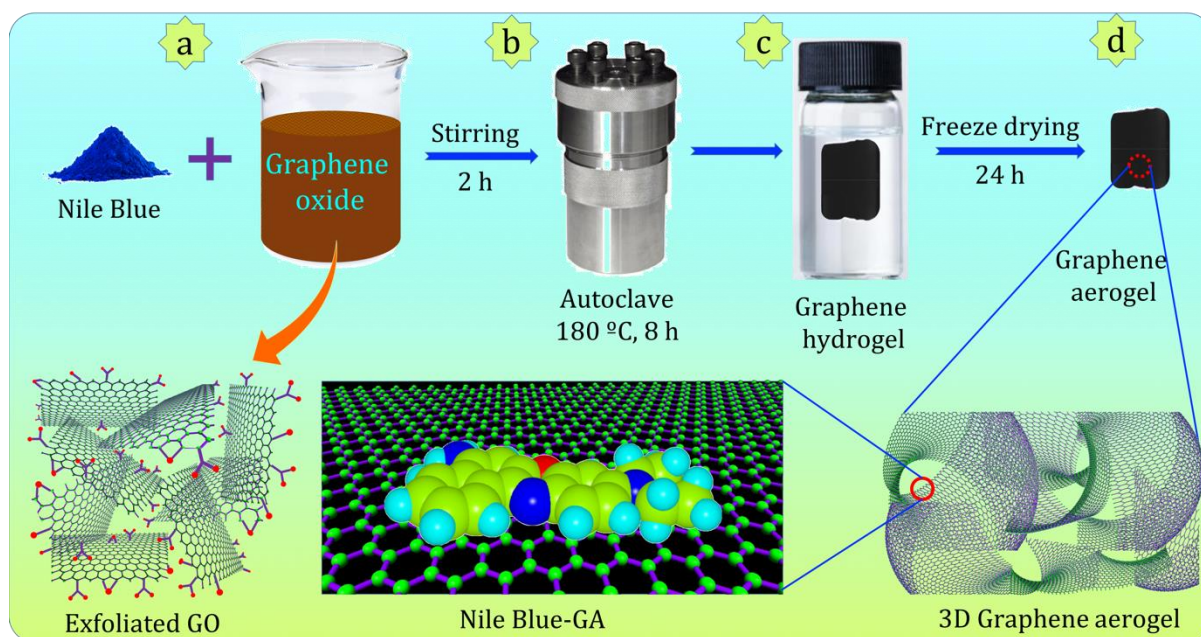


**Figure S1. Preparation of the NB-GA nanocomposite.** Schematic illustration of the hydrothermal synthesis route towards preparation of the Nile Blue functionalized 3D graphene aerogel (NB-GA). **a**, Addition of Nile Blue to the exfoliated graphene oxide suspension. The lower part of the panel is a schematic illustration of the GO basal plane and edges which are rich in epoxy, hydroxyl, carbonyl, and carboxyl groups, making them negatively charged when dispersed in aqueous electrolytes. **b**, Hydrothermal synthesis of NB-GA at 180 °C for 8 h. **c**, The graphene hydrogel floats in the solution, and leaves behind a clear and colorless solution. **d**, Freeze-dried graphene aerogel. The two bottom images show the 3D porous scaffold of the graphene aerogel and the  $\pi$ - $\pi$  stacking interactions between Nile Blue (that has a planar aromatic structure) and the graphene aerogel.

## 2. UV-vis and Fluorescence Spectroscopy Characterization of the Samples

Nile Blue is a cationic species, with a strong acceptor in the form of the charged iminium group in its structure, which induces a strong net dipole across the molecule. Because of the  $\pi$ -conjugated bridge between the electron donor and acceptor in Nile Blue, the  $sp^2$  character of the molecule is more pronounced than the other benzophenoxazine derivatives, and intramolecular charge transfer is more fluid.<sup>2</sup>

As shown in Fig. 2a (main text), the GO dispersion displays a maximum absorption at 228.5 nm, which is due to the  $\pi \rightarrow \pi^*$  transition of aromatic C=C bonds, along with a shoulder peak between 290 and 300 nm, which corresponds to the  $n \rightarrow \pi^*$  transition of the C=O bond.<sup>3</sup> The spectrum of diluted Nile Blue aqueous solution shows two strong absorption peaks at 282 nm and 635 nm, characteristics of aryl rings ( $\pi \rightarrow \pi^*$ ) and the  $n \rightarrow \pi^*$  transition of C=N bonds of Nile Blue in its monomeric form.<sup>4</sup> The spectrum of Nile Blue in water also exhibits a shoulder peak at ~590 nm that can be attributed to H-type dimer aggregation.<sup>5</sup> In the absorption spectrum of the NB-GO nanocomposite, absorption peaks of both GO and Nile Blue can be observed, indicating grafting of the Nile Blue molecules onto the GO surfaces. The sharp peak of GO in NB-GO (228.5 nm), suggests that the dimerization equilibrium is not significantly disrupted when Nile Blue is adsorbed onto a GO sheet.<sup>3</sup> Interestingly, as shown in Fig. 2a (main text), the intensity of the dimer peak at ~590 nm increases compared to that of the monomer peak at 635 nm, confirming that the equilibrium between the monomer and dimer forms of Nile Blue moves toward the dimer on GO due to the strong  $\pi$ - $\pi$  interactions.<sup>4</sup> In addition, the red shift (up to 35 nm) of the  $n \rightarrow \pi^*$  transition of the C=N bonds of Nile Blue to 670 nm provides evidence for delocalized  $\pi$ -electrons in the conjugated NB-GA macromolecules. GO nanosheets have a negative surface charge due to hydroxyl and carboxyl groups on the edges and basal-plane of the GO nanosheets. Thus, the cationic Nile Blue molecules are also adsorbed onto the GO surfaces due to electrostatic

attractive forces. A combination of these non-covalent attractive forces between Nile Blue and GO, holds them together in the nanocomposite, and the experimental results provide evidence for such interactions.

Note that, formation of the graphene aerogel from the graphene oxide dispersion proceeds *via* hydrothermal reduction of oxygen-containing functional groups, which leads to cross-linking of individual graphene oxide sheets to form the reduced graphene oxide hydrogel. After the preparation of the graphene oxide hydrogel, water molecules were removed from the carbon scaffolds *via* freeze-drying, without collapsing the solid structure, leading to the formation of the graphene aerogel.

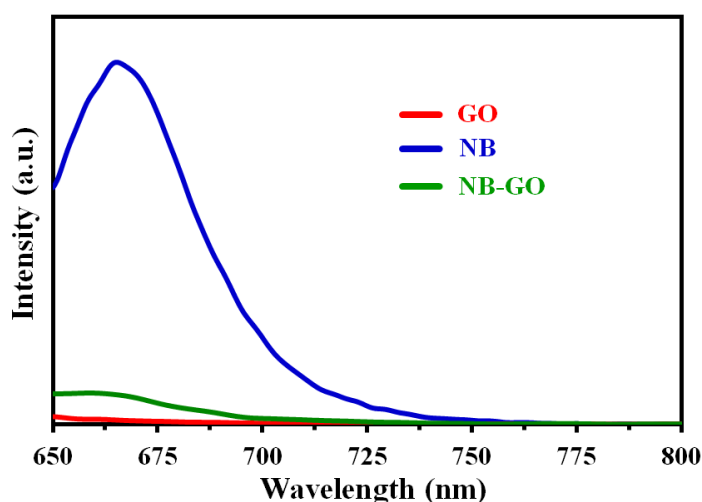


**Figure S2. Characterization by fluorescence spectroscopy.** Fluorescence spectra of free Nile blue (NB), graphene oxide (GO) and the Nile Blue-conjugated graphene oxide (NB-GO) samples in an aqueous solution.

We further confirmed formation of the NB-GA conjugate by fluorescence spectrometry. Free Nile Blue molecules show a maximum emission peak at 665 nm when excited at 636 nm (Figure S2). The pristine GO exhibits negligible fluorescence intensity in the investigated region. The Nile Blue molecules adsorbed on the GO nanosheets also exhibit a maximum emission peak at around 662 nm at the same excitation wavelength, but the fluorescence intensity is greatly diminished. Since the

concentration of Nile Blue was the same in both cases, the decrease in fluorescence intensity demonstrates that a large fraction of the excited Nile Blue molecules are quenched by the GO nanosheets. This observation can be attributed to the electronic coupling between Nile Blue molecules and GO nanosheets in the nanocomposite because of the effective charge or energy transfer *via*  $\pi$ - $\pi$  as well as electrostatic interactions between them.<sup>6, 7</sup> These results are in good agreement with other reported experiments on fluorescence properties of largely  $\pi$ -conjugated dye molecules in their free state or on graphene nanosheets.<sup>8, 9</sup>

To show that Nile Blue remains confined on GA after the hydrothermal synthesis, and does not leak out of the nanocomposite structure during operation, we recorded UV-vis absorption spectrum of electrolyte after 500 consecutive GCD cycles at a low current density of 2 A g<sup>-1</sup> (Figure S3). For comparison, the UV-vis absorption spectrum of a free Nile Blue sample (12.5  $\mu$ M in 1.0 M H<sub>2</sub>SO<sub>4</sub>) was also recorded. By comparing the two spectra, we notice that Nile Blue molecules do not leak out of the NB-GA nanocomposite structure under operation.

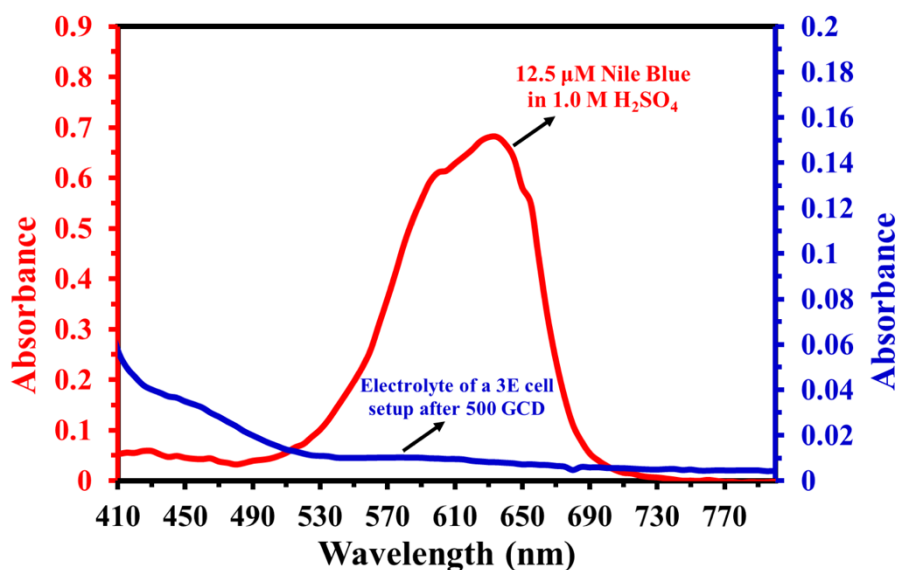


**Figure S3. UV-vis spectra showing that Nile Blue does not leak out of the nanocomposite structure under operation.** UV-vis absorption spectra of a 12.5  $\mu\text{M}$  Nile Blue in 1.0 M  $\text{H}_2\text{SO}_4$  solution (red spectrum) and the electrolyte of a 3E cell setup (1.0 M  $\text{H}_2\text{SO}_4$  solution) in which the electrode was immersed after completing 500 GCD cycles (blue spectrum). The blank was a 1.0 M  $\text{H}_2\text{SO}_4$  solution.

### 3. Nile Blue Leakage Test

The reaction of graphene aerogel (GA) with Nile Blue (NB) in the presence of water (W) is a competition among three types of interactions: solute-solute (NB-GA) interactions, solute-solvent (NB-W, GA-W, and NB-GA-W) interactions, and solvent-solvent (W-W) interactions. Figure S3 shows that Nile Blue remains confined on GA after the hydrothermal synthesis, and does not leak out of the nanocomposite structure during operation in an aqueous electrolyte. To provide additional evidence that the NB-GA interaction is stronger than the sum of the NB-W plus GA-W plus W-W terms, we dissolved the NB-GA nanocomposite in DMSO as a strong electron donor and polar aprotic solvent. Immediately after the addition of solvent, we observed a burst release of the Nile Blue molecules into the solvent and the solution turned wine red (Figure S4). Two main conclusions can be drawn from these observations: (i) If the Nile Blue

had been covalently conjugated to the graphene aerogel, the Nile Blue molecules would not have leaked out of the nanocomposite by solvation. (ii) Nile Blue molecules do not leak out of the NB-GA nanocomposite under operation in aqueous electrolytes. These results show that Nile Blue is preferentially conjugated to the graphene aerogel *via* non-covalent  $\pi$ - $\pi$  stacking interactions.

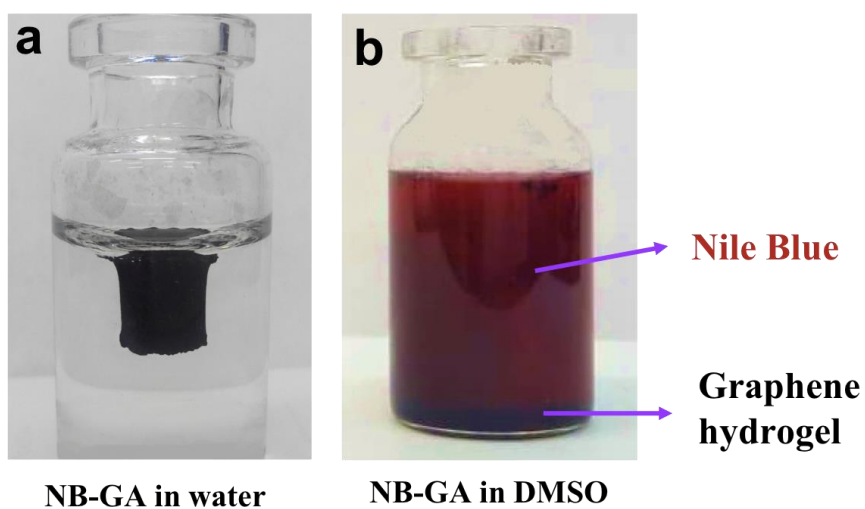


**Figure S4. Leakage test.** Photograph of an as-synthesized NB-GA nanocomposite in (a) water and (b) DMSO.

#### 4. FT-IR analysis

As shown in Fig. 2b (main text), in the spectrum of the graphene aerogel, the peaks at 1728  $\text{cm}^{-1}$  and 1641  $\text{cm}^{-1}$  correspond to the stretching vibrations of the C=O groups in carboxylic and carbonyl moieties, indicating the presence of COOH and COO functional groups on the surfaces of the graphene aerogel.<sup>10</sup> The FT-IR spectrum of free Nile Blue displays its heterocyclic ring stretching band ( $\nu$  C=C and C=N) at 1590  $\text{cm}^{-1}$ , the symmetric stretching band of CN at 1427  $\text{cm}^{-1}$ , and the symmetric deformation of -CH<sub>3</sub> at 1334  $\text{cm}^{-1}$ ,<sup>11</sup> which has also been reported for other similarly structured chemicals.<sup>12, 13</sup> The band between 2920 and 3200  $\text{cm}^{-1}$  is ascribed to the N-H symmetric stretching mode. The broad band at around 3440  $\text{cm}^{-1}$  can be mainly ascribed to adsorbed water as well as the asymmetric stretching vibration of N-H.<sup>14</sup> All the characteristic fingerprint peaks of Nile Blue and graphene aerogel are present in the FT-IR spectrum of the NB-GA nanocomposite. Note that, the stretching vibration of C-N in the amide group (typically at  $\sim$ 1260  $\text{cm}^{-1}$ ), which is commonly considered as demonstrative evidence for covalent conjugation of amine-containing dyes on GO, cannot be seen in the spectrum of NB-GA.<sup>10</sup> The FT-IR spectrum of NB-GA was slightly changed upon the adsorption of Nile Blue onto the graphene aerogel (e.g. the symmetric stretch of C-N at 1427  $\text{cm}^{-1}$  of Nile Blue mostly disappeared after its conjugation onto the graphene aerogel, and the heterocyclic ring stretching band at 1590  $\text{cm}^{-1}$  is broadened), demonstrating strong non-covalent  $\pi$ - $\pi$  interactions between Nile Blue and the graphene aerogel.<sup>10, 15</sup>

## 5. Raman Analysis

We conducted Raman analysis to provide additional evidence that Nile Blue molecules become conjugated with the graphene aerogel through  $\pi$ - $\pi$  stacking interactions. Figure S5 shows the Raman spectra of free Nile Blue, graphene oxide, as well as the NB-GA nanocomposite. Graphene oxide shows the well-known G-band, characteristic of  $sp^2$  hybridized carbon, at  $1592\text{ cm}^{-1}$ , and displays a peak at  $1361\text{ cm}^{-1}$  (D-band) originating from a disordered  $sp^3$  hybridized carbon. The summary of the characteristic peaks of Nile Blue is tabulated in Table S1. As shown in Figure S5, the Raman spectrum of the NB-GA nanocomposite shows the signatures of both Nile Blue and graphene oxide. Compared to graphene oxide, the NB-GA nanocomposite exhibits a clear G-band splitting that can be ascribed to the graphene 6-fold asymmetry breaking induced by the stacked Nile Blue molecules.<sup>16</sup> Moreover, all the bands are shifted toward lower wavenumbers compared to GO and the intensity of the 2D band also decreased. This also demonstrates noncovalent interactions of the graphene aerogel with  $\pi$ -stacking molecules,<sup>17, 18</sup> and is in a good agreement with the results of the FT-IR analysis.

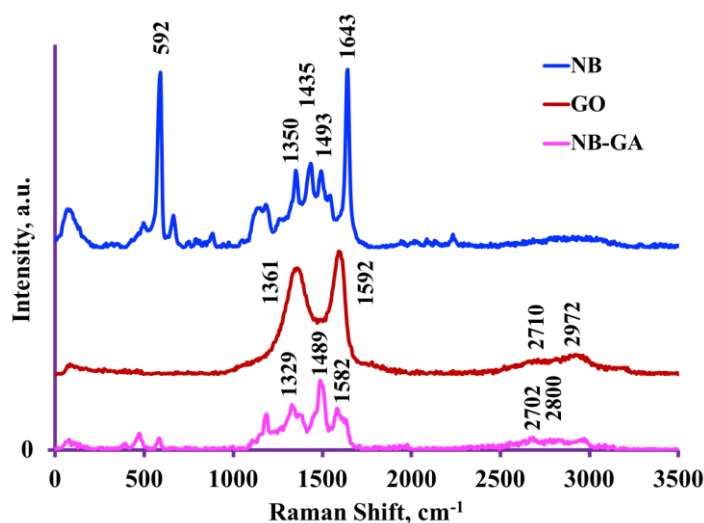


**Figure S5. Raman characterization of the Nile Blue-graphene aerogel interactions.** Raman spectra of free Nile Blue (blue), graphene oxide (dark red), and the NB-GA nanocomposite (magenta).

Table S1. Assignments of the Raman Bands of Nile Blue,<sup>19</sup> GO, and NB-GA

	Raman bands (cm <sup>-1</sup> )	Tentative assignments*
Nile Blue	1643	$\nu(\text{C6-C5}) + \nu(\text{C2-C3}) + \nu(\text{C1-N21})$ in-phase [ring-I (C=C) stretching]
	1493	$\delta(\text{C17H}) + \nu(\text{C4-N19}) + \nu(\text{C1-N21}) + \nu(\text{C2-C3})$
	1435	$\nu(\text{C-C})$ ring-IV + $\nu_s(\text{C4-N19-C7}) + \nu(\text{N21-C1}) + \nu(\text{C5-C6})$
	1350	$\nu(\text{C11-C12}) + \nu(\text{C-C})$ ring-IV + $\nu(\text{C1-N21}) + \nu_{as}(\text{C4-N19-C7}) + \beta(\text{C5H}) + \beta(\text{C9H})$
	592	$\nu_s(\text{C3-O20-C8}) + \nu_s(\text{C4-N19-C7})$ [ring-II breathing]
GO	1361	D-band
	1592	G-band
	2710	2D-band
NB-GA	1329	D-band
	1582	G-band
	2702	2D-band

\* Abbreviations used:  $\nu$ : stretching;  $\nu_s$ : symmetric stretching;  $\nu_{as}$ : asymmetric stretching;  $\delta$ : bending;  $\beta$ : in-plane bending. Assignments of the carbon atoms and rings of Nile Blue are based on Chart S1.

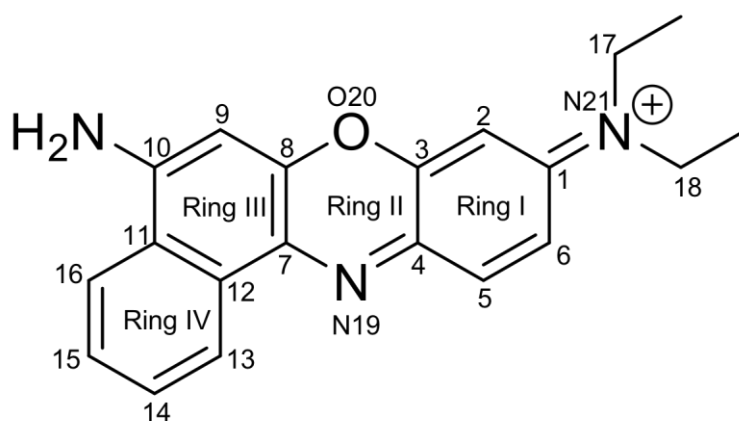


**Chart S1.** Chemical structure of Nile Blue with numbering for atoms and rings.

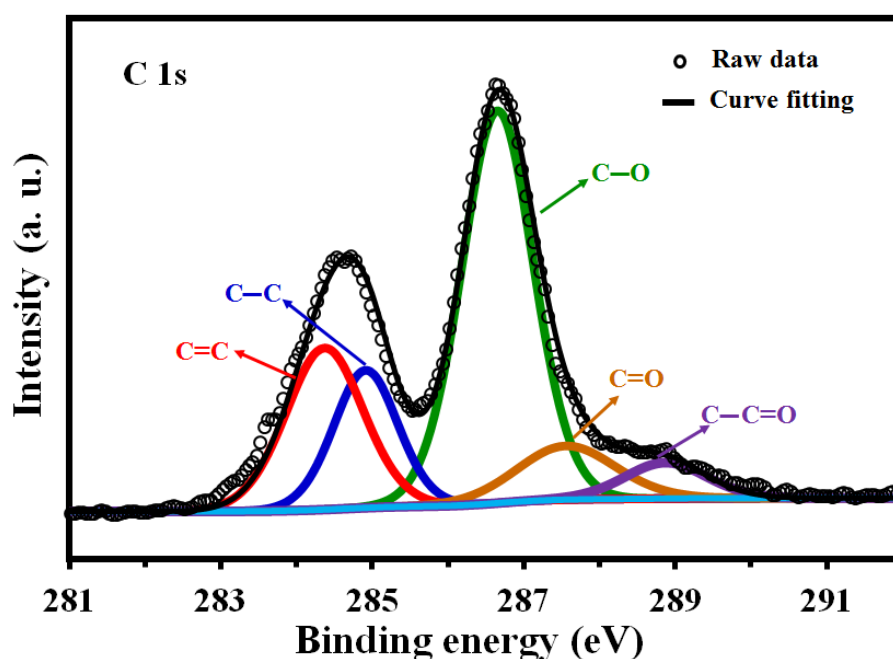
## 6. XRD Analysis

Figure 2c (main text) shows the XRD patterns of the as-prepared graphene oxide, graphene aerogel, and the NB-GA nanocomposite. The graphene oxide sample shows a high intensity peak at the diffraction angle ( $2\theta$ ) of  $11.4^\circ$  that is characteristic of the (001) reflection plane of graphene oxide. The calculated inter-planar spacing of graphene oxide is  $7.75 \text{ \AA}$ , which agrees well with previous reports.<sup>20, 21</sup> The large interlayer distance of graphene oxide indicates that planes of carbon atoms in graphite oxide are heavily decorated by oxygen-containing functional groups, which not only enlarges the interlayer distance of the sheets, but also makes the sheets hydrophilic. In the XRD pattern of the graphene aerogel sample, the intense diffraction peak at  $11.4^\circ$   $2\theta$  completely vanished and replaced with a broad and less intense diffraction peak at around  $2\theta$  of  $25.3^\circ$ . This can be ascribed to the (002) plane of graphene, demonstrating the extensive reduction of graphene oxide during the hydrothermal synthesis process.<sup>22,</sup> <sup>23</sup> The (002) reflection plane of the NB-GA nanocomposite shows a shift to a slightly higher  $2\theta$  value, which indicates an increase in ordering of the graphene sheets and partial restoration of the graphitic structure due to the  $\pi$ - $\pi$  interactions with Nile Blue.

## 7. XPS analysis

XPS survey spectra of the as-prepared graphene oxide, graphene aerogel, and NB-GA samples are shown in Fig. 2d (main text). The characteristic peaks of carbon (C 1s) and oxygen (O 1s) are observed in the survey spectra of all three samples. Comparing the survey XPS spectrum of graphene oxide with that of graphene aerogel and the NB-GA nanocomposite, it can be clearly seen that the oxygen content of the graphene aerogel and the NB-GA nanocomposite is significantly lower than that of graphene oxide, which demonstrates the successful reduction of the oxygen-containing functional groups of graphene oxide by the hydrothermal treatment.<sup>24</sup>

Deconvolution of the core-level C 1s spectrum of GO (Figure S6) shows four types of carbon bonds: C=C/C-C (284.6 eV), C-O (285.6 eV), C=O (286.5 eV) and O-C=O (287.8 eV). After reduction, these peaks are greatly diminished because most of the oxygen-containing functional groups are successfully removed from the NB-GA surfaces (Fig. 2e, main text). In addition, the remarkable increase in the amounts of the C=C components of the graphene aerogel and the NB-GA nanocomposite, which can be obtained from the peak at 284.6 eV, suggests that carbon atoms with  $sp^2$  hybridization are mostly restored during the hydrothermal process.<sup>25</sup> This was further confirmed by a broad shakeup satellite peak at the binding energy of 290 eV. Another peak in the C 1s spectrum of NB-GA appears at 285.8 eV, corresponding to C–N bonds in Nile Blue molecules, conjugated to the graphene sheets (Fig. 2e, main text).



**Figure S6. XPS characterization of GO.** Deconvoluted core level XPS spectra of graphene oxide, C 1s.

The N 1s core-level can be decomposed into three peaks (Fig. 2f, main text). The binding energies defined in 397.8, 399.4, and 401.6 eV are attributed to heterocyclic

nitrogen atoms ( $=N-$ ), amino nitrogen atoms ( $-NH_2$ ) and nitrogen cationic radical ( $N^+$ ), respectively, which demonstrate the non-covalent stacking of Nile Blue to reduced graphene oxide nanosheets in the NB-GA nanocomposites.<sup>3</sup>

## 8. BET/BJH Analyses

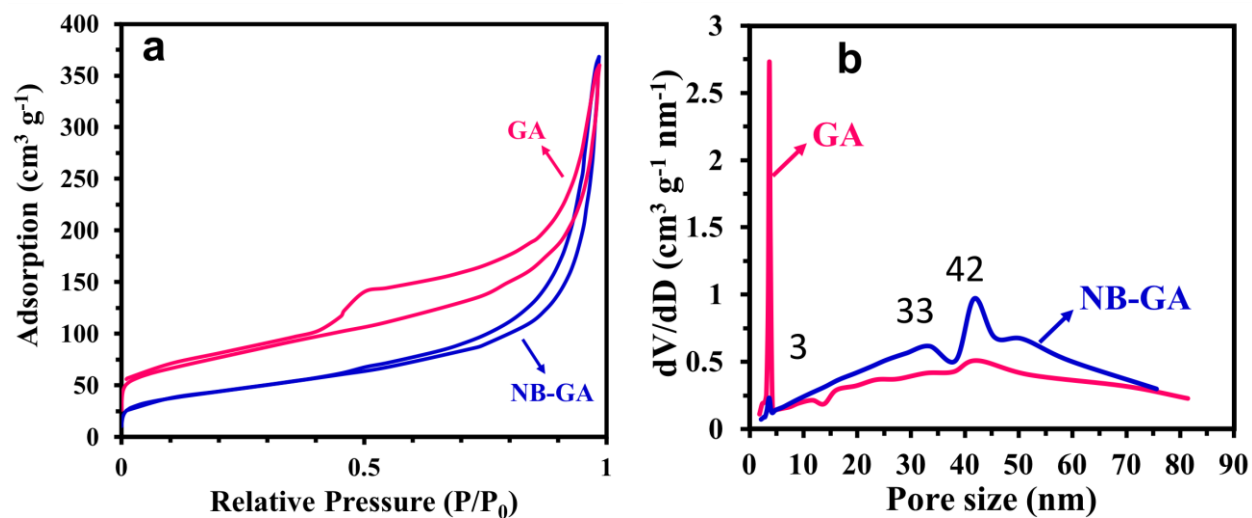


**Figure S7. BET and BJH analyses.** (a) Nitrogen adsorption and desorption isotherms and (b) BJH pore size distributions of the graphene aerogel and the NB-GA nanocomposite.

## 9. Electrochemical Characterization of the NB-GA Nanocomposite at Different Electrolytes

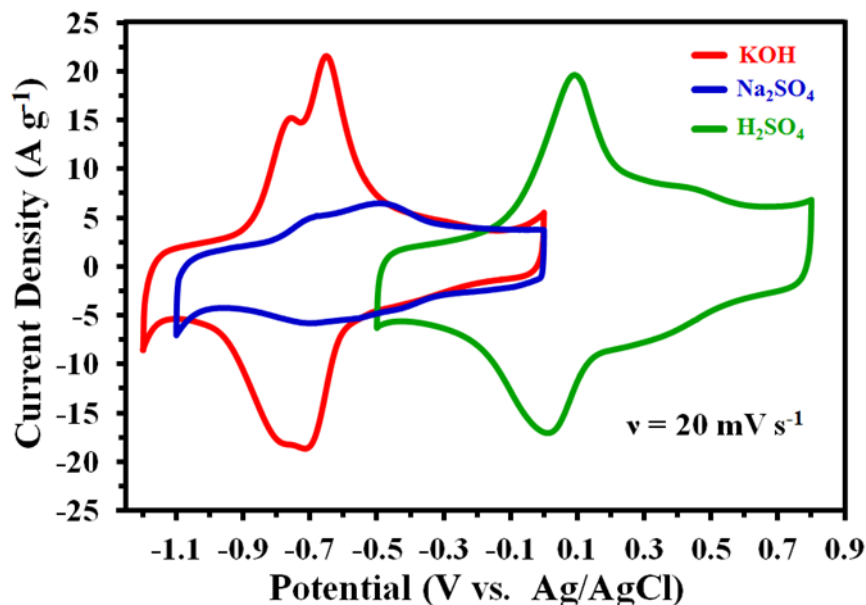


**Figure S8. Electrochemical performances of NB-GA electrode at different electrolytes.** Cyclic voltammograms of NB-GA electrode at a scan rate of  $20 \text{ mV s}^{-1}$  in alkaline (1.0 M KOH, red curve), neutral (1.0 M Na<sub>2</sub>SO<sub>4</sub>, blue curve), and acidic (1.0 M H<sub>2</sub>SO<sub>4</sub>, green curve) electrolytes.

In an alkaline electrolyte (Figure S8, red curve), the CV curve of the NB-GA nanocomposite electrode shows a pair of reversible redox peaks at around  $-0.65 \text{ V}$  superimposed on a large capacitive current. A linear dependence of peak current with scan rate (discussed later on) indicates that Nile Blue molecules are successfully conjugated to the graphene aerogel surfaces. Redox reactions also show near-symmetry in the cathodic and anodic peaks with  $\Delta E_p$  of  $38.9 \text{ mV}$  at a sweep rate of  $20 \text{ mV s}^{-1}$ , demonstrating an improved reversibility in the system. Additionally, the voltammogram displays an anodic pre-peak and a cathodic post-peak at low scan rates. The emergence of a pre-peak to the oxidation peak of Nile Blue can be considered as evidence for

stronger electrostatic adsorption of the positively charged oxidation products at the negatively charged graphene aerogel surface. The appearance of pre/post-peaks can also be attributed to the immobilization of some Nile Blue molecules at energetically different sites such as edges or defect sites on the basal plane of the graphene aerogel.<sup>26</sup> With increasing scan rate,  $\Delta E_p$  increases and the two peaks merge to form one broad peak located midway between the position of the pre-peak and the main peak. The electrochemical behavior of Nile Blue tethered to the graphene aerogel displays additional hump peaks at more positive potentials (around  $-0.3$  V), demonstrating that the conjugated Nile Blue molecules possibly undergo two separate, energy-resolved redox reactions.<sup>27</sup> The redox couple at around  $-0.3$  V has also been attributed to Nile Blue dimers and/or polymers.<sup>28</sup> We also investigated the electrochemical behavior of the NB-GA nanocomposite electrode in a  $\text{Na}_2\text{SO}_4$  electrolyte to find a way of making it a usable electrode active material for neutral aqueous electrolyte supercapacitors (Figure S8, blue curve). The CV curve shows almost the same trend as in alkaline electrolyte, but the peak currents are greatly diminished. However, no pre/post-peaks were observed in the acidic electrolyte, indicating that both oxidized and reduced species are strongly adsorbed onto the graphene aerogel surfaces (Figure S8, green curve).<sup>29</sup> In the same way, the hump peaks at more positive potentials (around  $0.43$  V) can be ascribed to Nile Blue dimers and/or polymers. Considering the molecular factors linked to the pseudocapacitive performance of amino-containing aromatic molecules adsorbed onto graphene-based materials,<sup>30</sup> it is also likely that  $-\text{NH}_2$ ,  $-\text{NH}-$ , and  $-\text{N}^+$  functional groups of the NB are redox-active in  $\text{H}_2\text{SO}_4$ , whereas  $-\text{NH}-$ , and  $-\text{N}^+$  functional groups are mainly active in KOH electrolyte.

It should also be noted that the overall energy storage performance not only depends on the electrode active materials, but also on the electrolyte. Generally, the use of aqueous

electrolytes in energy storage devices is more suitable than organic electrolytes because of lower cost, longer life time, lower internal resistance, non-flammability, and non-toxicity. We studied the electrochemical performance of the NB-GA electrodes in 1.0 M aqueous electrolyte solutions (KOH, H<sub>2</sub>SO<sub>4</sub>, and Na<sub>2</sub>SO<sub>4</sub>) that have been commonly used in energy storage devices. The differences in capacitive performances in different electrolytes can be attributed to the differences in compatibility of ion-size with pore-size, charge transfer resistance, ionic radius, ionic mobility, and molar ionic conductivity of the ions (Table S2) as well as the wettability of the electrode materials in the electrolyte. The large capacitance observed in the H<sub>2</sub>SO<sub>4</sub> electrolyte can be attributed to the lower cationic radius, higher ionic mobility and molar ionic conductivity of the H<sup>+</sup> ions. On the other hand, the relatively lower capacitance in the Na<sub>2</sub>SO<sub>4</sub> electrolyte can be attributed to the larger radius, lower ionic mobility and molar ionic conductivity of Na<sup>+</sup> ions compared to those of H<sup>+</sup> ions. Although K<sup>+</sup> ions are bigger than H<sup>+</sup> ions, the increased capacitance in KOH can be attributed to the higher ionic mobility and molar ionic conductivity of OH<sup>-</sup> ions as well as the increased wettability of graphene-based materials in 1.0 M KOH compared to the other two electrolytes.<sup>31</sup> On the other hand, current, which is expressed in amperes (= Coulombs/second), is a quantitative expression of how fast a redox reaction occurs. The Faradaic current is directly related to the rate of the reaction taking place at that interface. Therefore, when we measure the Faradaic current, we are also measuring the rate of a redox reaction. Since the magnitude of current is directly proportional to the rate of the electrochemical reaction, it is reasonable to conclude that the oxidation rate of Nile Blue is lower in the neutral Na<sub>2</sub>SO<sub>4</sub> electrolyte compared to the other two electrolytes.

Table S2. Characteristic Parameters of Ions in Aqueous Electrolytes<sup>32</sup>

ions	Ionic radius (Å)	hydrated sphere radius (Å)	Ionic mobility $\times 10^{-8}$ ( $\text{m}^2 \text{s}^{-1} \text{V}^{-1}$ )	Molar ionic conductivity ( $\text{ms m}^2 \text{mol}^{-1}$ )
$\text{H}^+$ ( $\text{H}_3\text{O}^+$ )	0.021	2.80	36.23	34.96
$\text{Na}^+$	1.02	3.58	5.19	5.01
$\text{K}^+$	1.38	3.31	7.62	7.35
$\text{OH}^-$	0.46	3.00	20.64	19.91
$\text{SO}_4^{2-}$	2.30	3.79	8.29	16.00

## 10. pH Dependent Electrochemistry of Nile Blue

The shift of peak potentials with change in pH is a characteristic feature of proton-coupled electron transfer reactions. Generally, for a redox couple in which  $m$  protons and  $n$  electrons are transferred ( $Ox + ne^- + mH^+ \leftrightarrow Red$ ), the peak potential,  $E$ , varies with pH based on Equation S1:<sup>33</sup>

$$E = E^0 + \frac{RT}{nF} \ln \frac{[Ox]}{[Red]} - \frac{2.303 mRT}{nF} pH \quad (S1)$$

According to this expression, the slope of a plot of  $E$  versus pH should be  $-2.303 mRT/nF$ . The slope in  $E$  versus pH plot of 59 mV/pH shows that the redox reaction mechanism involves an equal number of electrons and protons (e.g.  $2e^-/2H^+$ ), if the number of protons involved in the redox reaction is twice the number of electrons (e.g.  $1e^-/2H^+$ ), the plot would have a slope of 118 mV/pH unit, a slope of 29 mV/pH suggests that the number of electrons is twice the number of protons (e.g.  $2e^-/1H^+$ ), and when the potential is independent of pH (slope = 0 mV/pH), no proton is coupled into the electron transfer process. Figure S9a shows the pH-dependence of the  $E$  values of the NB-GA nanocomposite over the pH range from 1.0 to 14.0. Since two electrons are involved in the redox reaction of Nile Blue, the number of protons transferred was determined by using Equation S1.

The detailed CV scans in the pH range from 1.25 to 4.00 revealed two iso-potential points ( $E_{iso}$ ) in which the peak at 0.06 V (pH 1.25) transforms into a peak centered at -0.40 V (pH 4). The

$E_{iso}$  ( $-0.15$  V in the anodic scans (Figure S9b) and  $-0.50$  V in the cathodic scans vs. Ag/AgCl) corresponds to a change in the dominant reaction with changing the pH (with a transition centered at pH 2.25). The  $E_{iso}$  is representative of a system consisting of two forms of a redox species, which are interconvertible so that the total quantity remains constant. The peak potentials shifted cathodically with increasing pH, probably due to the change in electronic properties and promoted electron acceptor ability of the Nile Blue by forming an extended conjugated system.<sup>34, 35</sup>

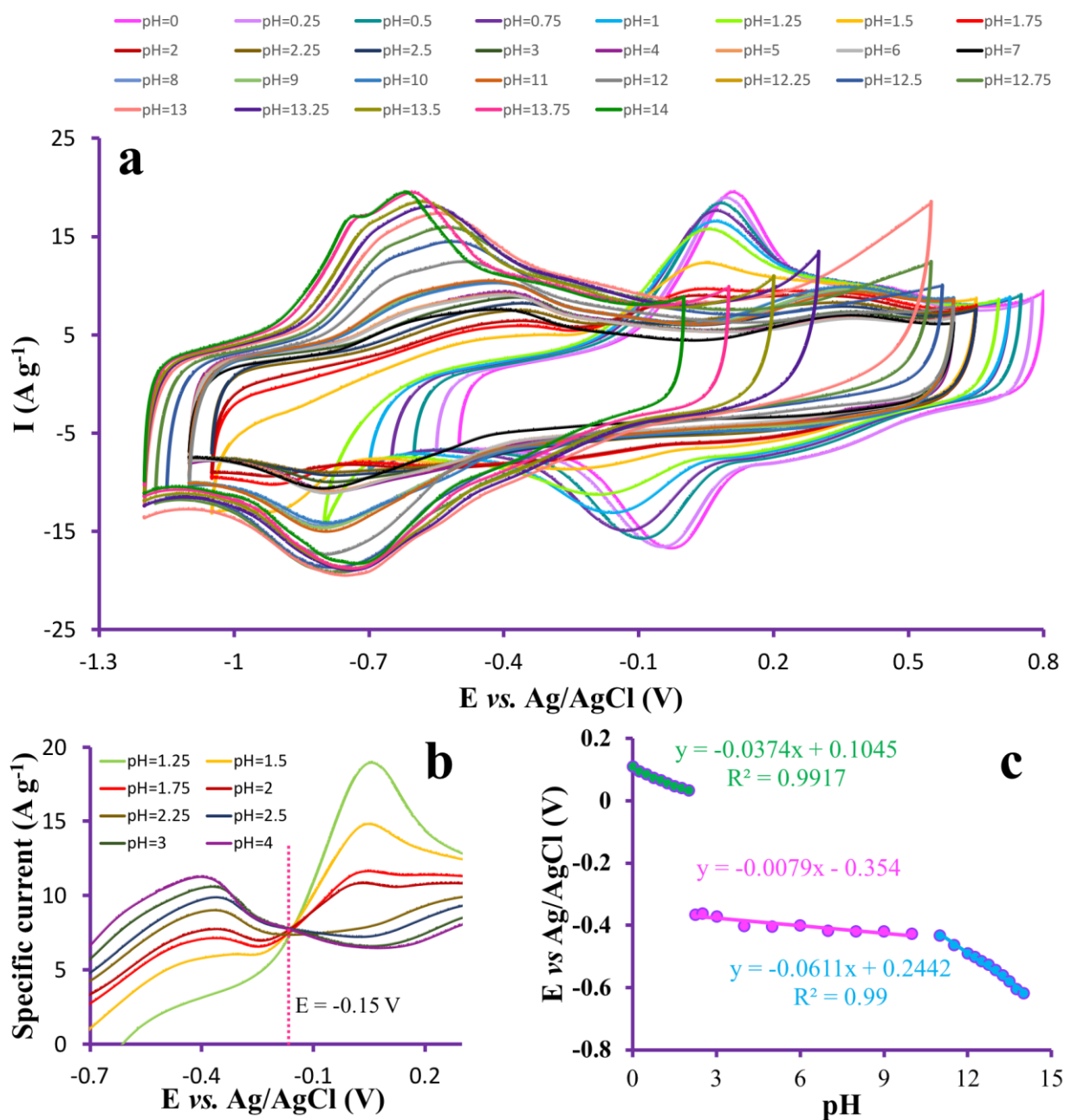


**Figure S9.** (a) CVs of the NB-GA nanocomposite electrode in un-buffered aqueous solution at various pH's. Scan rate = 20 mV s<sup>-1</sup>. (b) Scale expansion of the CV profiles of the NB-GA nanocomposite electrode in the anodic scan showing an iso-potential point. (c)  $E_{pa}$  vs. pH plot for the NB-GA nanocomposite in un-buffered aqueous electrolytes at various pH's (obtained from the CVs of panel a).

As can be seen from the  $pH$ - $E$  profile (Figure S9c), there are three linear segments that are described by the following equations:

$$E = 0.1045 - 0.0374 \text{ pH} \quad (R^2 = 992, 0 \leq \text{pH} \leq 2) \quad (\text{S2})$$

$$E = -0.345 - 0.0079 \text{ pH} \quad (2 < \text{pH} < 11) \quad (\text{S3})$$

$$E = 0.2442 - 0.0611 \text{ pH} \quad (R^2 = 0.99, 11 \leq \text{pH} \leq 14) \quad (\text{S4})$$

The peak potential of Nile Blue shifts  $\sim 37$  mV/pH for  $0 \leq \text{pH} \leq 2$  and  $\sim 61$  mV/pH for  $11 \leq \text{pH} \leq 14$ . Given that from the literature the overall oxidation of Nile Blue is known to be a  $2e^-$  process, this behavior of the Nile Blue redox couple clearly indicates involvement of  $2e^-$  and  $1H^+$  for  $0 \leq \text{pH} \leq 2$  and  $2e^-$  and  $2H^+$  for  $11 \leq \text{pH} \leq 14$ . The independence of the peak potential on pH for  $2 < \text{pH} < 11$  implies that no protons are involved in the redox reaction of the NB-GA nanocomposite in the non-buffered aqueous electrolytes.

Nile Blue in the solution phase is reported to undergo a complex electrochemical oxidation mechanism as summarized in Chart S2.<sup>36-39</sup> However, based on our findings, the reaction scheme for Nile Blue in the NB-GA nanocomposite is inconsistent with previous reports that assume involvement of  $2e^-$  and  $2H^+$  for acidic electrolytes and  $2e^-$  and  $1H^+$  for alkaline electrolytes with the transition centered near pH 6.0. This is especially unlikely in a  $H_2SO_4$  electrolyte as it requires Nile Blue to be deprotonated, which is not possible given that its  $pK_a$  is  $\sim 10$ .<sup>40</sup> Analogous to the redox reaction of hydroquinone on graphene nanoflakes<sup>41</sup> as well as on a glassy carbon electrode modified by  $-COOH$  bearing diazonium salt of 4-aminophthalic acid,<sup>42</sup> a  $2e^-/1H^+$  mechanism would, however, be possible in the presence of an additional source of protons inside the nanocomposite, such as the  $COOH$ -terminating groups of the graphene aerogel. In a strongly acidic electrolyte ( $\text{pH} < 2$ ), there would be protons readily available *via* hydroxyl ( $-OH$ ) and carboxylic acid ( $-COOH$ ) groups on the basal plane and edges of the graphene aerogel to participate in proton transfer reactions (Chart S3) and to provide hydrogen bonding sites, thereby providing a situation that substantially differs from those in the bulk electrolyte. Likewise, in a strongly alkaline electrolyte ( $\text{pH} > 11$ ), deprotonated ( $-COO^-$ ) groups would participate in proton transfer reactions, thus proton-coupled electron transfer reactions would proceed *via* a  $2e^-/2H^+$  mechanism (Chart S3). The process of dimerization and its redox reactions would likely be the same as that outlined in Chart S2.

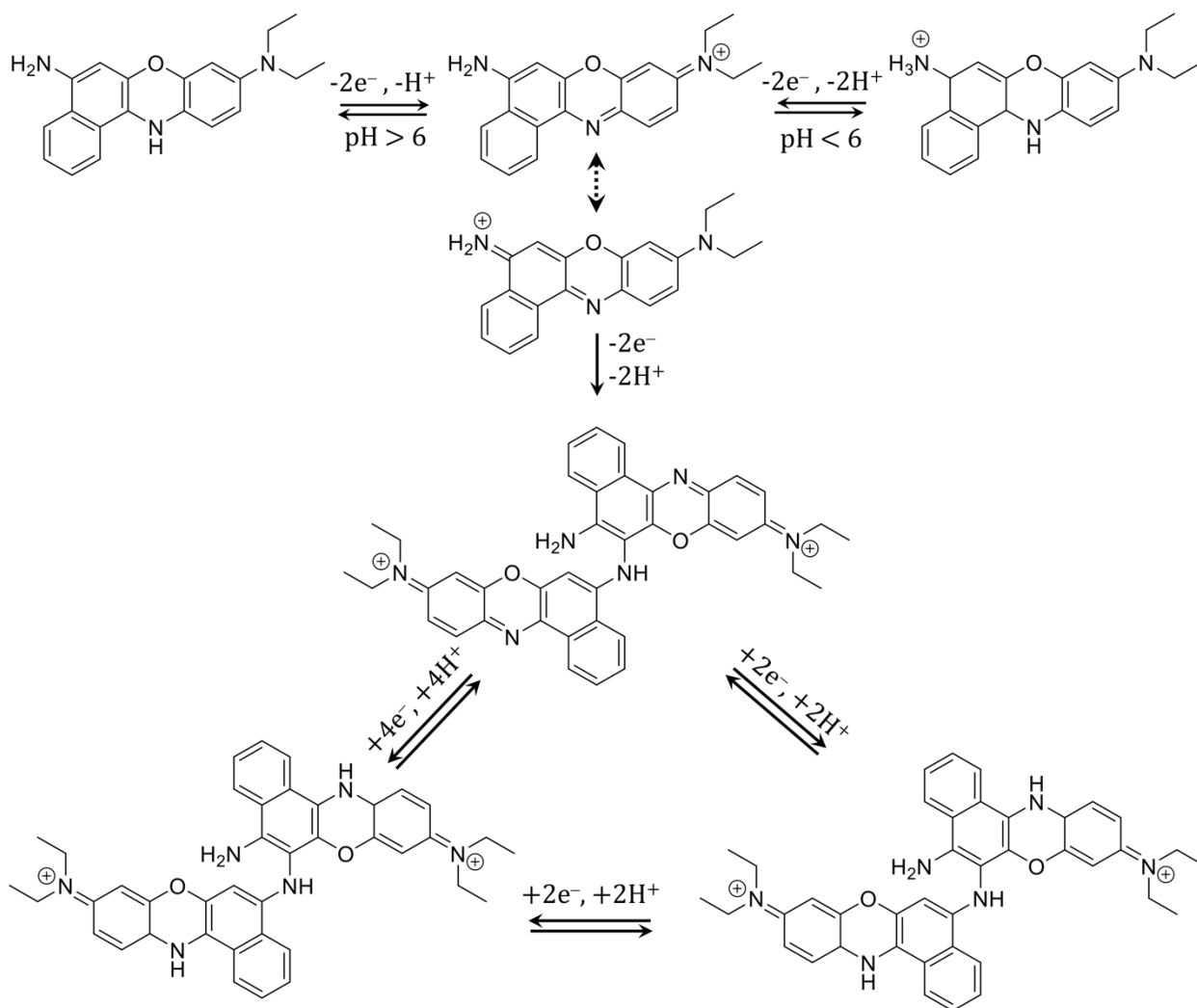


**Chart S2. Mechanisms of Nile Blue redox behavior in solution phase.**<sup>36-39</sup> Possible mechanisms of Nile Blue redox reactions in solution (at different pH values) and the synthetic pathway for Nile Blue dimers.

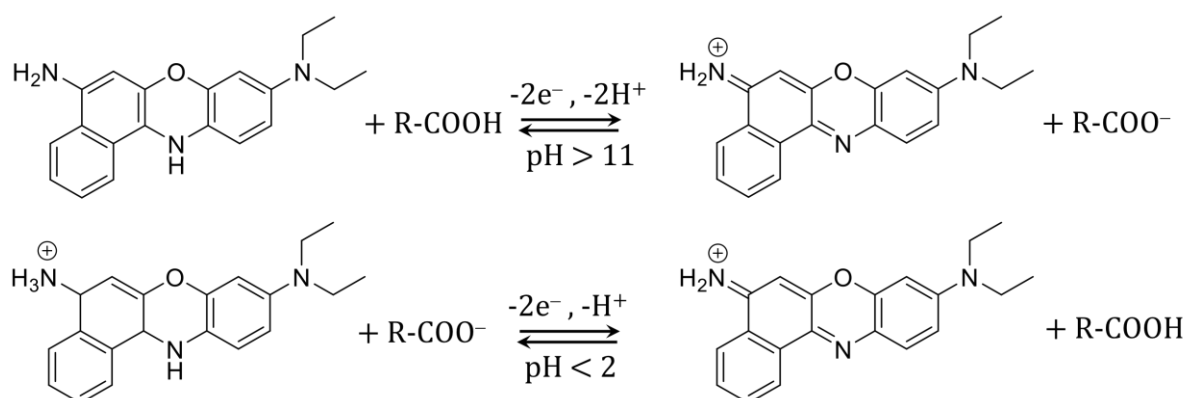


**Chart S3. Proposed mechanisms of Nile Blue redox behavior in the NB-GA nanocomposite.** Possible redox mechanisms of Nile Blue confined onto the graphene aerogel at different pH values of the un-buffered electrolytes.

## 11. Optimization of the Nile Blue content

We optimized the Nile Blue content of the nanocomposites by varying the mass ratio of NB to GO from 0.2 to 0.6, and recorded the CV curves (at a scan rate of  $20 \text{ mV s}^{-1}$ , over the potential range from  $-0.5$  to  $0.8 \text{ V}$ ) as an analytical signal (Figure S10). With increasing mass ratio of Nile Blue to GO up to 0.4, the integrated area of the CV curves increases as well. When the mass ratio of Nile Blue:GO is 0.4, the highest specific capacitance of  $371 \text{ F g}^{-1}$  is obtained. By further increasing the Nile Blue content in the nanocomposite, the mass-normalized capacitance of the electrode starts to decrease. This is mainly due to the following reasons: (1) inefficient conjugation of the Nile Blue molecules on the GA surfaces, (2) reduced conductivity of the composite due to the addition of non-conducting Nile Blue molecules, (3) a decrease in the interlayer distance of the GA sheets through electronic interactions, and (4) blockage of the pores, or some combination of all four.

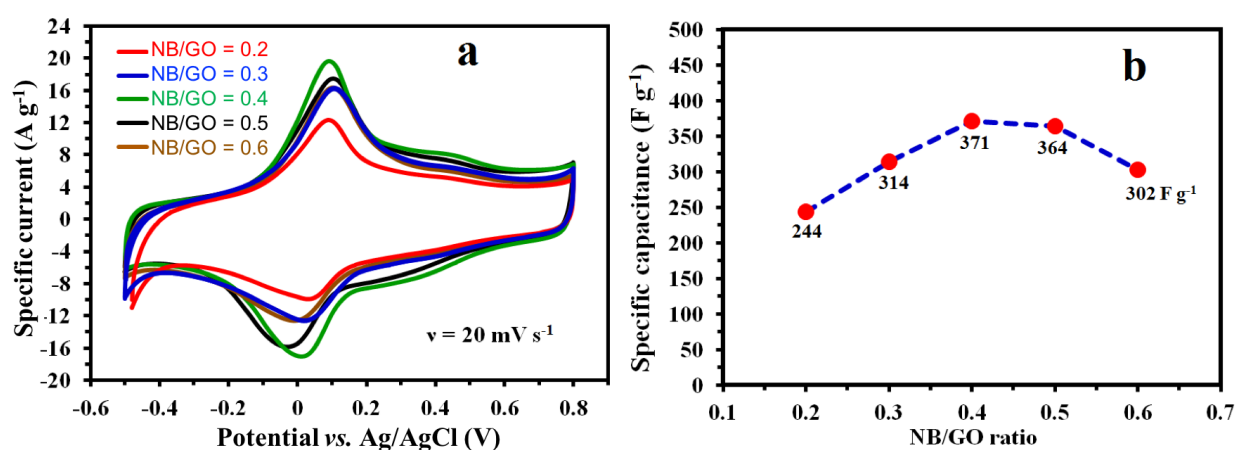


**Figure S10. Optimization of the Nile Blue:GO mass ratio.** **a**, CVs of the NB-GA electrode (at  $20 \text{ mV s}^{-1}$ ) with different Nile Blue:GO wt% ratios from 0.2 to 0.6. **b**, The change in specific capacitance as a function of the wt% ratios of Nile Blue to GO for the as-synthesized NB-GA electrodes.

## 12. Electrochemical Studies in a Three-Electrode Cell Setup

The fascinating pseudocapacitive properties of the NB-GA nanocomposite are attributed to the synergistic and combinatorial benefits of Nile Blue and the three-dimensional hierarchical structure of the graphene aerogel. As a fascinating effect in the solid state,  $\pi$ - $\pi$  stacking interactions are even more favorable when one of the species is  $\pi$ -electron rich and the other one is  $\pi$ -electron deficient.<sup>43</sup> The very strong  $\pi$ - $\pi$  stacking interactions between Nile Blue (as a positively charged electron-deficient species) and GA (as an electron-rich unit) help explain the unique features of the nanocomposite and the resulting large electronic coupling. In addition, the hierarchically porous structure of GA has several advantages for improving the supercapacitive performance of the nanocomposite: first, the macropores serve as ion-buffering reservoirs, shortening the ion diffusion pathways and boosting the electrochemical kinetics; second, the mesopores provide more channels for ion transport, ensuring smaller ion-transport resistance; and third, the micropores increase the effective surface area and accommodate charges.<sup>44</sup> Thus, a rationally designed carbon nanostructure with an excellent balance between microporosity, mesoporosity and macroporosity is highly desirable to attain an energy storage device with an exceptional performance.

The specific capacitance of the NB-GA electrode was calculated to be  $371 \text{ F g}^{-1}$  at  $20 \text{ mV s}^{-1}$  (in a  $1.0 \text{ M H}_2\text{SO}_4$  electrolyte), which is considerably higher than the sum of the capacitances of the Nile Blue ( $19 \text{ F g}^{-1}$ ) and the graphene aerogel electrodes ( $192 \text{ F g}^{-1}$ ), i.e.  $19 \times 19.8\% + 192 \times 80.2 = 157.7 \text{ F g}^{-1}$ , indicating a strong synergistic effect between the two compounds (note that 19.8 and 80.2 are the percentages of Nile Blue and graphene aerogel in the NB-GA nanocomposite). The NB-GA nanocomposite electrode also shows a specific capacitance of  $145 \text{ F g}^{-1}$  in a neutral ( $1.0 \text{ M Na}_2\text{SO}_4$ ) aqueous electrolyte, which is a significantly high value for graphene-based materials in neutral

electrolytes. In an alkaline (1.0 M KOH) electrolyte, the NB-GA nanocomposite electrode exhibits a high specific capacitance of 364 F g<sup>-1</sup> (at 20 mV s<sup>-1</sup>). Figure S11a,b show typical CV curves of the NB-GA electrode measured at various scan rates ranging from 1 to 200 mV s<sup>-1</sup>. With increasing scan rate from 1 to 200 mV s<sup>-1</sup>, the shape of the CV curves has no obvious change, indicating fast charge transfer through the graphene aerogel network and rapid ion transport through the porous structure of the nanocomposite. There are energy rich electrons in the graphene aerogel that could form  $\pi$ - $\pi$  stacking interactions with Nile Blue molecules. Consequently, the redox reaction of Nile Blue at the NB-GA nanocomposite is facilitated and proceeds *via* fast redox reaction kinetics that translates into an excellent capacitive performance.

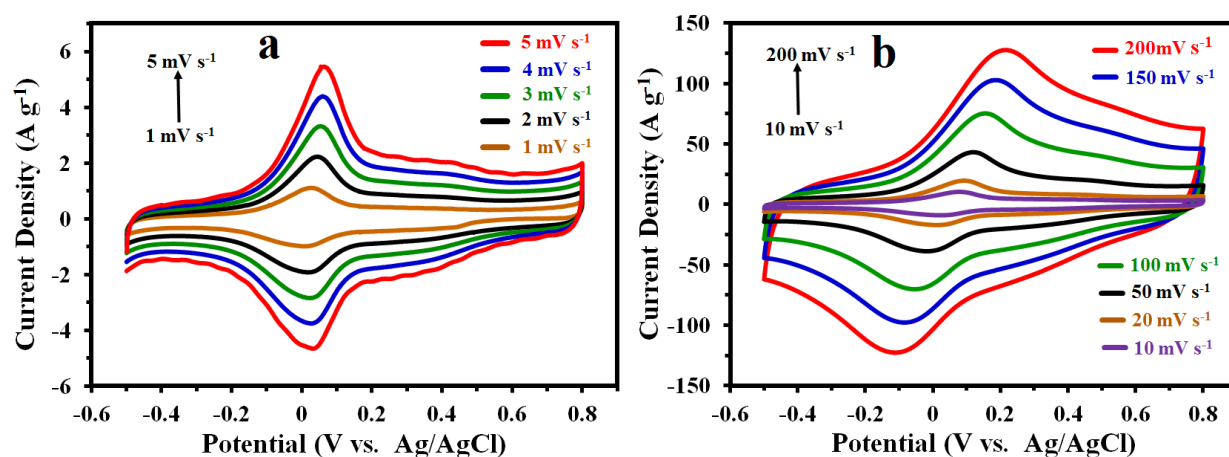


**Figure S11. Scan rate study of the NB-GA electrode.** CV curves of an NB-GA electrode at different scan rates in 1.0 M H<sub>2</sub>SO<sub>4</sub> solution. **a**, 1 to 5 mV s<sup>-1</sup> and **b**, 10 to 200 mV s<sup>-1</sup>.

Figure S11 clearly shows that the oxidation and reduction peak currents increase with increasing scan rate. From the slopes of the linear plots of  $I$  vs.  $v$  (Figure S12) the surface concentration of the Nile Blue can be obtained based on Laviron's equation as follows:<sup>45</sup>

$$i_p = \frac{n^2 F^2 \nu A \Gamma}{4RT} \quad (\text{S5})$$

where  $n$  represents the number of electrons,  $A$  is the surface area ( $\text{cm}^2$ ),  $\Gamma$  is the surface coverage of the Nile Blue ( $\text{mol cm}^{-2}$ ) and other symbols have their usual meaning. The surface concentration of Nile Blue on the graphene aerogel was calculated to be  $1.69 \times 10^{-10} \text{ mol cm}^{-2}$  of BET area and  $5.22 \times 10^{-7} \text{ mol cm}^{-2}$  of geometric area, which is higher than that of Nile Blue adsorbed onto a graphite electrode ( $4.19 \times 10^{-9} \text{ mol cm}^{-2}$  to  $9.72 \times 10^{-9} \text{ mol cm}^{-2}$ )<sup>46</sup> or covalently immobilized on self-assembled thiol-monolayer modified gold electrodes ( $6.64 \times 10^{-11} \text{ mol cm}^{-2}$ ).<sup>47</sup>

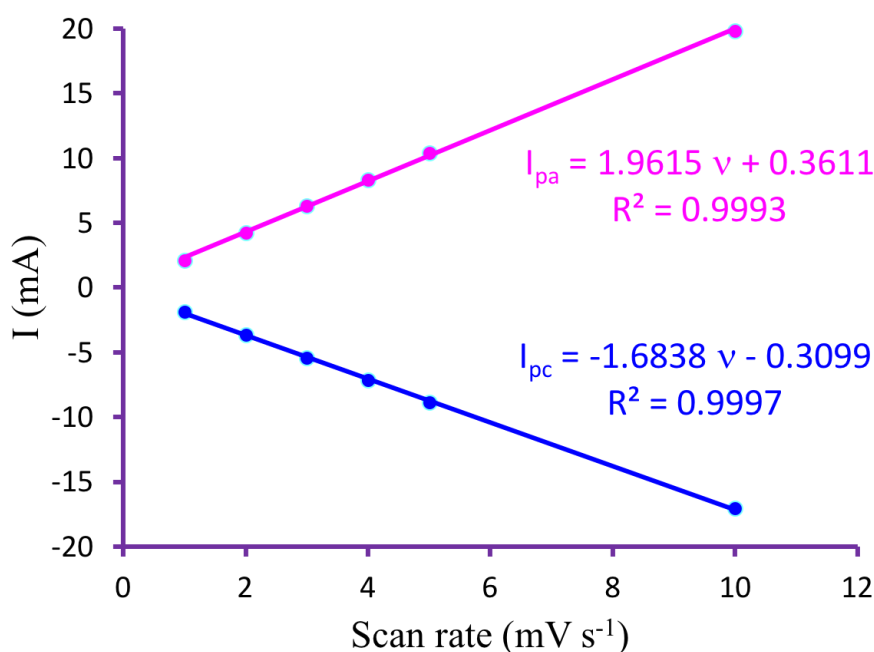


**Figure S12. Calculation of the Nile Blue surface coverage by Laviron's method.** Plot of the anodic and cathodic peak currents vs. scan rate at lower values of scan rate. The data are obtained from the CVs presented in Figure S11. (Note: peak currents are not normalized.)

### 13. EIS Characterization of the NB-GA Electrode

Detailed insights into the processes taking place at the NB-GA nanocomposite electrodes were provided by the EIS studies. Figure S13 shows Nyquist plots of the NB-GA nanocomposite electrode over the frequency range from 100 kHz to 10 mHz at various electrode potentials in a 1.0 M H<sub>2</sub>SO<sub>4</sub> solution. The equivalent circuit model fit to the experimental data is shown in the inset to Figure S13b. In the equivalent circuit, *ESR* represents the equivalent series resistance, comprised of the ionic resistance of the electrolyte and the electronic resistance of the electrode. Constant phase elements (CPE1-2) are used in the equivalent circuit in place of a capacitor to compensate for non-ideal behavior of the electrodes. *RI* can be ascribed to the electrolyte impedance in the larger interparticle porosity of the NB-GA nanocomposite, as well as the solid-electrolyte interface (SEI) layer formed on the surface of the electrode.<sup>48-50</sup> *R2* can be attributed to the electrolyte impedance in small channels connecting the larger pores, as well as the parallel porous sublayers of different thicknesses, along with the ionic or so-called diffusion resistance of the electrolyte.<sup>48, 50, 51</sup> The overlapping semicircles can also be ascribed to interconnected bi-spherical pores for which the effects of each sphere can be observed at different frequencies; the semicircle at higher frequencies can be attributed to the first sphere and the semicircle at the middle frequencies originates from the second (deeper) sphere.<sup>52</sup> Note that, since the large semicircles at the middle frequency region are almost potential independent, they cannot be attributed to charge transfer resistance that decreases with an increase in applied potential.<sup>53</sup> The inclined line in the middle-to-low frequency region, namely the slope of the 45° portion right after the second semicircles, can be attributed to the Warburg impedance. Looking at Figure S13b, the high frequency ends of the plots intercept the *Z<sub>re</sub>* axis at nearly the same point due to similar characteristics of the electrodes at different potentials. The Nyquist plot of the NB-GA electrode (Fig. 3e, main text) shows a very small *ESR*

value of  $\sim 0.28 \Omega$  in the high frequency region and a near vertical line at low frequencies. The two overlapping semicircles can be attributed to the fact that ion transport in the electrolyte and ion insertion into the NB-GA nanocomposite take place simultaneously throughout the porous electrode. Interestingly, the Warburg impedance of the NB-GA electrode is  $0.265 \Omega \text{ s}^{-1/2}$ , which is a significantly low value and indicates only a small contribution from diffusion-controlled redox processes in the energy storage performance of the NB-GA nanocomposite electrode. This traces back to the efficient charge/ion transport through the porous structure of the NB-GA nanocomposite. Here, the slope of the line at low frequencies is very steep, indicating that the charging process is controlled by electric double layer formation.

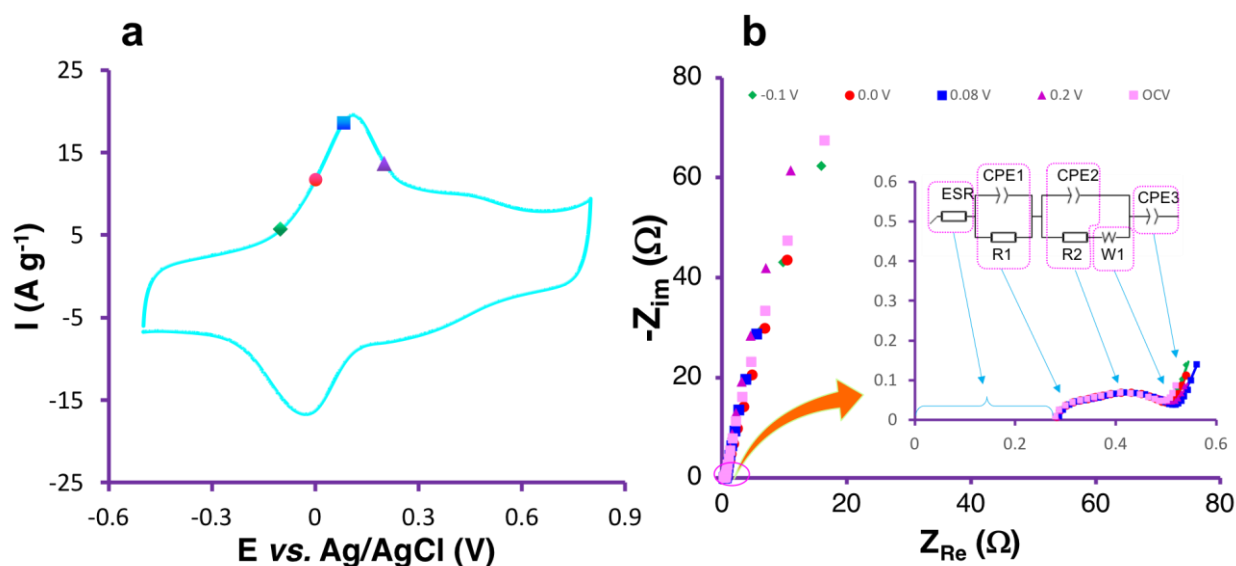


**Figure S13. EIS characterization of the NB-GA nanocomposite electrode at different potentials.** (a) CV of the NB-GA nanocomposite electrode in 1.0 M  $\text{H}_2\text{SO}_4$  electrolyte in which the potentials of -0.1, 0.0, 0.08, and 0.2 V are marked. (b) A series of Nyquist plots measured at different potentials of the CV. Insets: The proposed equivalent circuit as well as a magnified high-frequency region. The points are the real EIS data and the lines are the fits to the experimental data.

At low frequencies, the phase angle of the NB-GA electrode is  $-81^\circ$ , very close to the  $-90^\circ$  for ideal capacitors (Figure S14). In addition, a log-log plot of the impedance magnitude versus frequency for the NB-GA electrode shows a slope of about  $-0.92$  in the low frequency region, which is close to  $-1.0$  expected for ideal capacitors. The RC time constants for the NB-GA electrodes, obtained from the Bode phase plot at the phase angle of  $45^\circ$  is  $176$  ms, showing a much faster response time than many other conventional activated carbon-based electrochemical capacitors.<sup>54</sup> The nanocomposite electrode exhibits a very low  $iR$  drop even at a high specific current of  $100 \text{ A g}^{-1}$ . This characteristic is a consequence of: (i) the high conductivity of the nanocomposite, and (ii) the low ion transport resistances of the materials, which are two key factors to achieve high-rate energy storage materials.

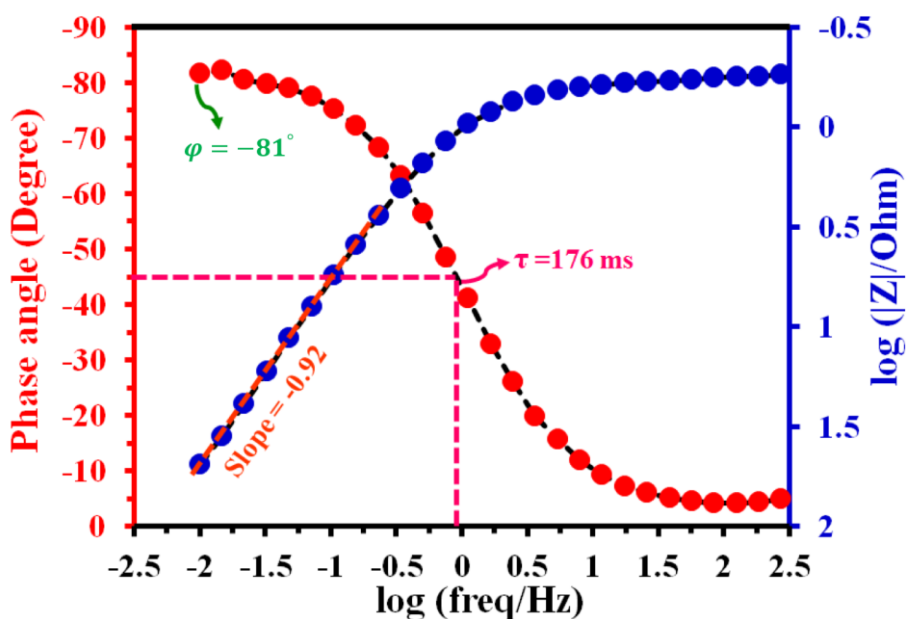


**Figure S14.** EIS characterization of the NB-GA electrode. The Bode plot (phase angle and the  $\log |Z|$ , i.e. total impedance, vs. log frequency) for the NB-GA electrode over a frequency range from 100 kHz to 0.01 Hz.

#### 14. Decoupling the Contribution of Capacitive and Non-capacitive Faradaic Processes

The total stored charge in supercapacitors consists of three major components: 1) capacitive non-Faradaic charge storage (known as EDLC), 2) capacitive Faradaic charge storage (referred to as pseudocapacitance), and 3) non-capacitive Faradaic charge storage (denoted as battery-like behavior).<sup>55</sup> According to the theory of the voltammetric response, the CV curve of an electrode can be described as:<sup>56</sup>

$$i(v) = av^b \quad (S6)$$

and the equation can be rearranged as:

$$\log i(v) = \log a + b \log(v) \quad (S7)$$

where  $i$  is the current (A),  $v$  is the potential sweep rate ( $V s^{-1}$ ), and  $a$  and  $b$  are arbitrary coefficients. In the above-mentioned equations, A  $b$ -value of 0.5 indicates that the current is controlled by semi-infinite diffusion (i.e. battery-like behavior), and a  $b$ -value of 1 demonstrates that surface redox processes follow fast redox kinetics (i.e. capacitive charge transfer process). Hybrid systems exhibit a  $b$ -value in between. Using Equation (S7), the  $b$ -value can be determined from the slope of the plot of  $\log i$  versus  $\log v$  as shown in Figure S15. The calculated  $b$ -value is 0.91, very close to 1, suggesting a typical capacitive behavior with fast surface ion adsorption/desorption and reversible redox reactions. To quantitatively resolve the contribution from capacitive and battery-like processes in the total charge, the following general relationship which holds for any material regardless of the charge transfer process can be used:<sup>57</sup>

$$i(V) = k_1v + k_2v^{1/2} \quad (S8)$$

where  $k_1$  and  $k_2$  denote the coefficients for capacitive and battery-like currents, respectively. According to Equation (S8), for a redox reaction limited by semi-infinite linear diffusion, the  $i(V)$  varies with  $v^{1/2}$ , and for a capacitive process, the  $i(V)$  varies directly with  $v$ . Equation (S8) can be rearranged as:

$$i(V)/v^{1/2} = k_1 v^{1/2} + k_2 \quad (\text{S9})$$

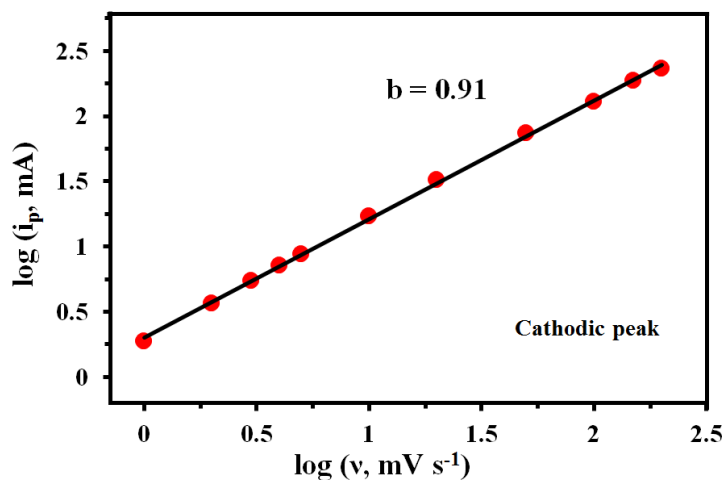


**Figure S15.** The  $\log(i)$  versus  $\log(v)$  plot of the cathodic peak currents.

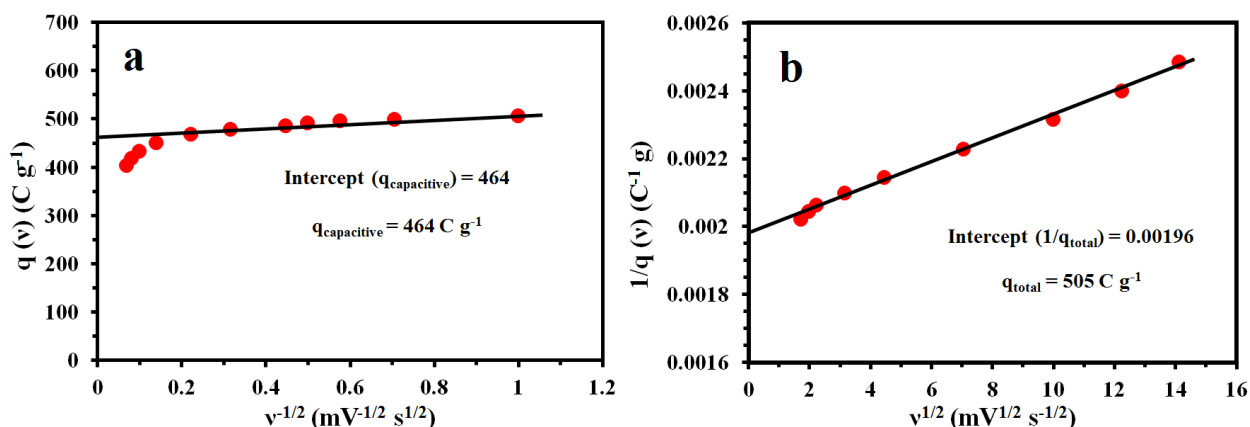


**Figure S16.** Trasatti analysis, utilizing the dependence of the voltammetric charge storage on the sweep rate. **a**, As  $v \rightarrow \infty$ , extrapolation of the charge storage versus the  $v^{-1/2}$  curve gives the capacitive charge storage ( $q_{\text{capacitive}}$ ). **b**, As  $v \rightarrow 0$ , extrapolation of the inverse capacity versus the  $v^{1/2}$  curve gives the total charge ( $q_{\text{total}}$ ).

Here, Trasatti's method is used to mathematically deconvolute the contribution from capacitive and diffusion-controlled processes in the total charge stored.<sup>58, 59</sup> According to Trasatti's theory, we can separate the total stored charge ( $q$ ) into two parts, (1) the charge arising

from the surface capacitive charge storage processes ( $q_c$ ), and (2) the charge arising from diffusion-controlled ion intercalation processes ( $q_d$ ):

$$q(v) = q_{capacitive} + q_{diffusion} \quad (S10)$$

which can be rewritten as:

$$q(v) = q_{capacitive} + \alpha(v^{-1/2}) \quad (S11)$$

where  $q(v)$  is the voltammetric charge calculated by integration of the area under the CV,  $q_{capacitive}$  is the capacitive charge (both from double layer and pseudo-capacitive processes), and  $\alpha v^{-1/2}$  indicates charge storage associated with semi-infinite diffusion, where  $\alpha$  is a constant and  $v$  is the sweep rate. The  $q_{capacitive}$  value corresponding to surface-dominant processes is obtained at an infinite potential sweep rate ( $v \rightarrow \infty$ ), due to capacitive charge storage processes that will be almost always constant at any sweep rate, whereas charge storage processes coming from diffusion-controlled redox processes are highly dependent on the sweep rate. Thus, at sufficiently high sweep rates, more of the diffusion-controlled redox processes are excluded from contributing to the charge storage. Therefore, according to Equation (S11),  $q_{capacitive}$  can be estimated from the extrapolation of  $q(v)$  to  $v = \infty$  from the plot of  $q(v)$  versus  $v^{-1/2}$ . As shown in Figure S16a, the value of  $q_{capacitive}$  is estimated to be  $464 \text{ C g}^{-1}$ . Otherwise, the maximum total charge density ( $q_{tot}$ ) is obtained when  $v \rightarrow 0$ , because the electrochemical reaction time-scale is long enough to allow the full contribution from diffusion-controlled processes. Since  $q(v)$  increases linearly with  $v^{-1/2}$ , it is reasonable to expect that  $1/q(v)$  decreases linearly with  $v^{1/2}$  as follows:

$$1/q(v) = 1/q_{tot} + \alpha(v^{1/2}) \quad (S12)$$

Therefore according to Equation (S12),  $q_{total}$  was calculated to be  $505 \text{ C g}^{-1}$  from the extrapolation of the trend line of  $1/q(v)$  to  $v = 0$  from the  $1/q(v)$  versus  $v^{1/2}$  plot, as shown in Figure S16b. Consequently, the difference between the total charge ( $q_{tot}$ ) and the capacitive

charge storage ( $q_{\text{capacitive}}$ ) gives the charge associated with the diffusion-controlled processes ( $q_{\text{diffusion}}$ ).

$$q_{\text{diffusion}} = q(\nu) - q_{\text{capacitive}} \quad (\text{S13})$$

Using Equation (S13), we can conclude that  $q_{\text{diffusion}}$  is just  $41 \text{ C g}^{-1}$ . The ratio of the capacitive charge storage to the total charge storage is 91%, which is in excellent agreement with the analysis mentioned in the main text and indicating that the majority of the charge storage occurs *via* a non-diffusion controlled manner in our system.

**Table S3.** Comparison of the NB-GA Electrode with other Pseudocapacitive Materials Based on their Contribution to Capacitive Charge Storage

Electrode materials	Capacitive contribution (%)	Scan rate (mV s <sup>-1</sup> )	Mass loading (mg cm <sup>-2</sup> )	Ref
NS-GNS	74	1	1.8	60
Ti <sub>3</sub> C <sub>2</sub> T <sub>x</sub> /CF	75	50	0.8	61
$\alpha$ -MoO <sub>3</sub>	70	0.1	-	62
MoO <sub>2</sub> -RGO hybrid	83.5	1	1.0	63
mesoporous CeO <sub>2</sub>	70	0.5	-	64
mp-MoS <sub>2</sub> (Li-ion electrolytes)	91	1	0.036	59
mp-MoS <sub>2</sub> (Na-ion electrolytes)	82			
reduced $\alpha$ -MoO <sub>3-x</sub> (R-MoO <sub>3-x</sub> )	75	1	0.04	65
Templated Nanocrystal TiO <sub>2</sub>	65	10		66
TiO <sub>2</sub> Nanoparticles	55	0.5	0.01-0.015	67
V <sub>2</sub> O <sub>5</sub> /CNT nanowire	70	1	1-3	68
2D-TiS <sub>2</sub>	85	1	0.34	69
b-MoS <sub>2</sub>	62	1	1.0	70
nc-MoS <sub>2</sub>	83			
GF-SnS	84	0.8	~1.0	71
MoS <sub>2-x</sub> Se <sub>x</sub> /GF	68.4	0.4	1.95	72
Na <sub>2</sub> Ti <sub>3</sub> O <sub>7</sub> @C HHSs	88.3	10	1.0	73
SnO <sub>2</sub> @P@GO	63.2	0.1	1.5-2.0	74
Ni <sub>3</sub> S <sub>2</sub> -Ni	81	1	-	75
GF@Fe <sub>2</sub> O <sub>3</sub>	78	50	-	76

<b>Lig/PEDOT</b>	66	100	-	77
<b>G-NCs</b>	50	2	0.8	78
<b>Nanoflower-like WO<sub>3</sub> (NFL-WO<sub>3</sub>)</b>	83	100	3.31	79
<b>MnO<sub>2</sub>-MNC</b>	90.4	10	6.0	80
<b>mesoporous MCNO-HNTs</b>	55.7	2	0.8-1.2	81
<b>HPCO</b>	83.2	1	1.5-2.0	82
<b>V<sub>2</sub>O<sub>5</sub>.nH<sub>2</sub>O</b>	51.3	1	2.0-3.0	83
<b>TiO<sub>2</sub>@MoO<sub>2</sub>-C</b>	60	1	0.7-0.8	84
<b>NVP-AHD</b>	64	5	-	85
<b>Mo<sub>1.33</sub>C MXene</b>	45	2	~1.0	86
<b>MnS-CT composites</b>	17.15	2	1.25	87
	61	20		
<b>NiMoO<sub>4</sub> nanoflakes</b>	60	1		88
<b>Thionine functionalized 3D graphene aerogel (Th-GA)</b>	93	1	2.0	15
<b>Nile Blue functionalized 3D graphene aerogel (NB-GA)</b>	93.4	2	2.0	This work

The capacitive-dominant NB-GA nanocomposite demonstrates excellent electrochemical performance as a negative electrode material in all acidic, neutral and alkaline aqueous electrolytes. The NB-GA nanocomposite has several distinct and beneficial features including: desirable electronic properties (since the non-covalent  $\pi$ - $\pi$  stacking interactions do not disrupt the  $sp^2$  structure and the extended  $\pi$ -conjugation on the graphene aerogel surfaces); a 3D hierarchical porous structure without structural collapse; the uniformity of the distributed Nile Blue species in between the graphene sheets; and the full exposure of active sites to the electrolyte. Such a conjugated product ensures the high electronic conductivity of the NB-GA nanocomposite, while the porous structure of the nanocomposite enables a fast transport of ions, thus leading to faster kinetics and higher utilization of active material. The NB-GA electrode exhibits specific capacitance of  $483 \text{ F g}^{-1}$  at  $1 \text{ A g}^{-1}$  in an  $\text{H}_2\text{SO}_4$  electrolyte, which is an extremely high value and quite rare for negative electrode materials.

To demonstrate robust stability and applicability of the NB-GA nanocomposite across a wide range of pH values, we designed a symmetric NB-GA || NB-GA supercapacitor along with asymmetric NB-GA ||  $\text{MnO}_2$  and NB-GA || LDH supercapacitors in acidic, neutral and alkaline electrolytes, respectively. The devices demonstrate excellent supercapacitive performances in all three kinds of electrolytes.

## 15. Electrochemical Properties of the NB-GA || NB-GA symmetric device

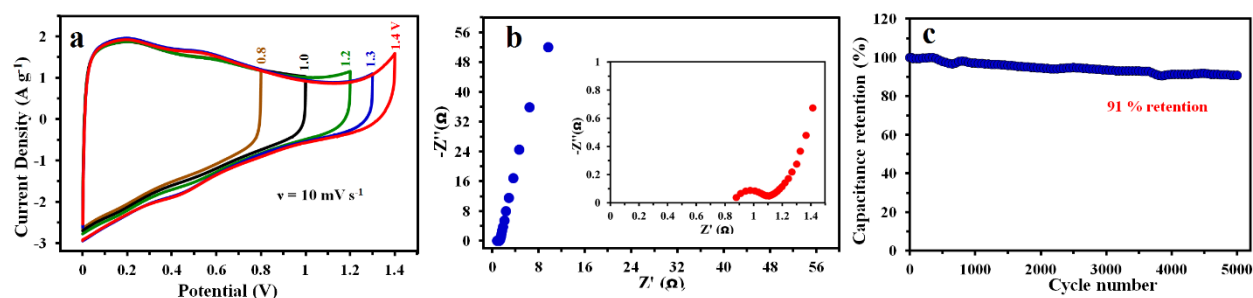


**Figure S17. Electrochemical evaluation of a NB-GA || NB-GA symmetric device in an aqueous 1.0 M H<sub>2</sub>SO<sub>4</sub> electrolyte. a,** CV curves of the NB-GA || NB-GA device at different potential windows ( $\nu = 50 \text{ mV s}^{-1}$ ). **b,** Nyquist plot of the NB-GA || NB-GA symmetric device in the frequency range from 100 kHz to 10 mHz. The inset shows the magnified high-frequency region. **c,** Long-term cycling stability of an NB-GA || NB-GA symmetric device over 5,000 consecutive GCD cycles at a current density of  $5 \text{ A g}^{-1}$ .

Figure S17a presents typical CV curves of the NB-GA || NB-GA symmetric device at a scan rate of  $10 \text{ mV s}^{-1}$  with different cutoff potentials from 0.8 to 1.4 V. As shown in Figure S17a, a small current leap appears at the end of the charging process when the potential exceeds 1.4 V. This can be attributed to the decomposition of H<sub>2</sub>O at high overpotentials that diminishes the Coulombic efficiency and stability of the device over successive cycles. Therefore, we selected an operating voltage window of 1.3 V for the symmetric NB-GA || NB-GA device, which is also in accordance with the potential window of the NB-GA electrode in a three-electrode system.

Figure S17b displays Nyquist plots of the NB-GA || NB-GA symmetric device in a frequency range from 100 kHz to 10 mHz. The semicircle at high frequency is followed by a near-vertical line at low frequency, which confirms a close to ideal capacitive behavior of the device. According to the Nyquist plot, the intercept of the imaginary part at the real axis, which represents the ESR, is  $\sim 0.88 \text{ } \Omega$ . The low value of ESR

demonstrates the low internal resistance of this device. The diameter of the semicircle at high frequencies, which represents  $R_{ct}$ , is also very small ( $0.24 \Omega$ ) for the NB-GA || NB-GA symmetric device, indicating fast reaction kinetics and excellent electrochemical activity of the nanocomposite.

Furthermore, the relationship between the specific current and specific capacitance of the NB-GA || NB-GA device is illustrated in Fig. 3j (main text). As can be seen, the NB-GA || NB-GA device shows a high rate capability (69% retention of the initial capacitance obtained at  $1 \text{ A g}^{-1}$  at a specific current of  $20 \text{ A g}^{-1}$ ), highlighting the good rate capability of the device. In addition, the Nyquist plot of the NB-GA || NB-GA symmetric device shows low resistance and good capacitive charge storage (Figure S17b).

Cycling stability is another important requirement that verifies practical applicability of a supercapacitor. We evaluated cycling capability of the NB-GA || NB-GA device by recording 5,000 continuous GCD cycles at a specific current of  $5 \text{ A g}^{-1}$ . As shown in Figure S17c, the symmetric NB-GA || NB-GA device retains 91% of its initial capacitance after 5,000 charge/discharge cycles which indicates excellent electrochemical stability.

## 16. Electrochemical Properties of the NB-GA || MnO<sub>2</sub> Asymmetric Device

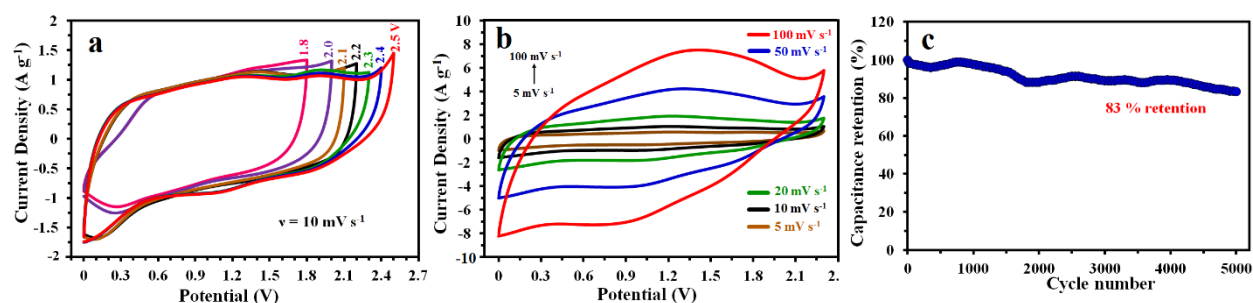


**Figure S18. Electrochemical evaluation of an NB-GA || MnO<sub>2</sub> asymmetric device in an aqueous 1.0 M Na<sub>2</sub>SO<sub>4</sub> electrolyte. a,** CV curves of an NB-GA || MnO<sub>2</sub> device at different potential windows from 1.8 V to 2.5 V ( $\nu = 10 \text{ mV s}^{-1}$ ). **b,** CV curves of the NB-GA || MnO<sub>2</sub> device at different scan rates. **c,** Long-term cycling stability of an NB-GA || MnO<sub>2</sub> asymmetric device over 5,000 consecutive GCD cycles at a current density of 5 A g<sup>-1</sup>.

An asymmetric supercapacitor architecture, assembled using two dissimilar electrode materials, allows the operating voltage window to be extended beyond the thermodynamic stability limit of water (i.e. 1.23 V), thereby, offering much higher energy and power densities.<sup>89</sup>

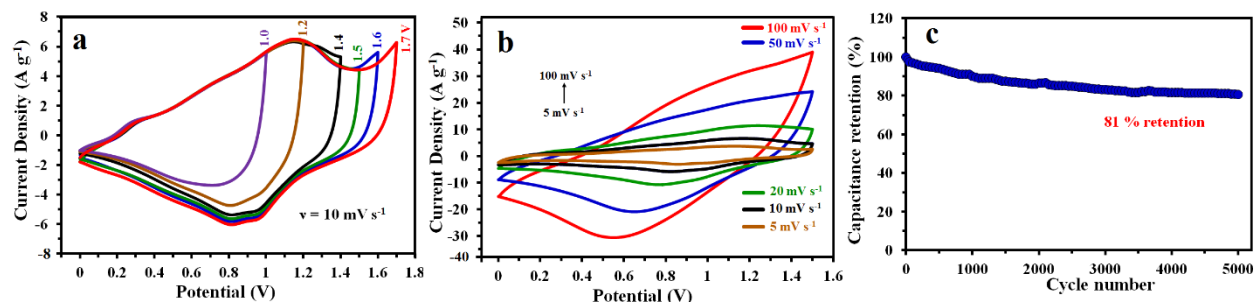
We recorded the CV curves of the NB-GA || MnO<sub>2</sub> asymmetric device at different potential windows (at a scan rate of 10 mV s<sup>-1</sup>) until the polarization trend of the electrolyte becomes very obvious (Figure S18a). Noticeable decomposition of water starts at an ultrahigh voltage of 2.5 V, more than two times wider than the thermodynamic breakdown window of water, and increases in rate as the voltage is increased. However, to ensure long-term stability of its operation, we limited the working voltage window of the NB-GA || MnO<sub>2</sub> device to 2.3 V. Figure S18b presents CV curves of the NB-GA || MnO<sub>2</sub> asymmetric device at various scan rates. Noticeably, the device retains the quasi-rectangular shape of the CV curves at different

scan rates ranging from 5–100 mV s<sup>-1</sup>, demonstrating a high rate capability and reversibility for the device.

A maximum specific capacitance of 75 F g<sup>-1</sup> was obtained at specific current of 1 A g<sup>-1</sup>. The relationship between specific capacitance and specific current of the NB-GA || MnO<sub>2</sub> asymmetric device is illustrated in Fig. 4j (main text). As can be seen, a 24% capacitance retention at a high specific current of 20 A g<sup>-1</sup> provides additional evidence for good rate capability.

In order to investigate the long-term cycling stability of the device, we performed over 5,000 GCD cycles at a specific current of 5 A g<sup>-1</sup>. As shown in Figure S18c, NB-GA || MnO<sub>2</sub> asymmetric device retained 83% of their initial capacitance indicating good cycling stability for the device.

## 17. Electrochemical Properties of the NB-GA || LDH Asymmetric Device



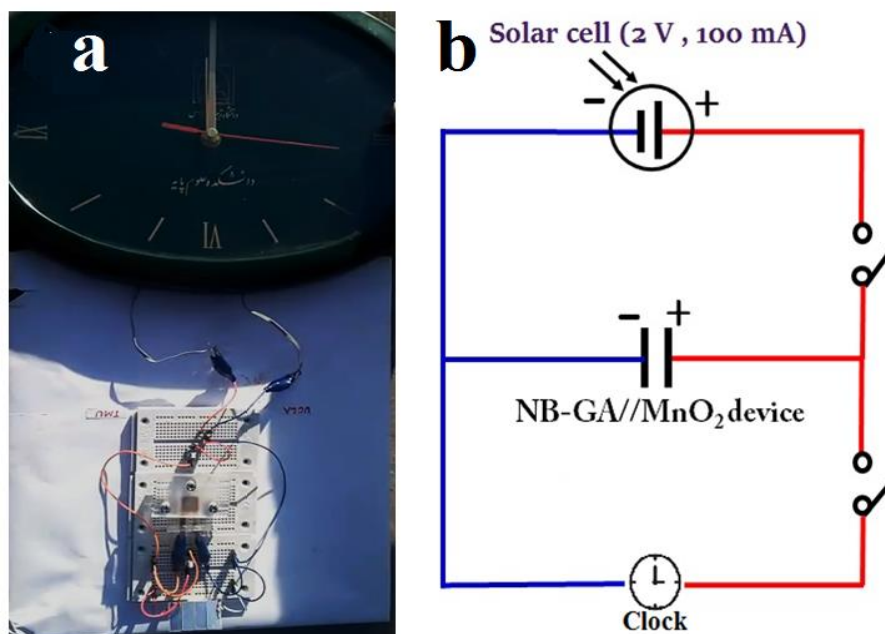
**Figure S19.** Electrochemical evaluation of an NB-GA || LDH asymmetric device in an aqueous 1.0 M KOH electrolyte. **a**, CV curves of an NB-GA || LDH device at different potential windows ranging from 1.0 to 1.7 V ( $v = 10 \text{ mV s}^{-1}$ ). **b**, CV curves of the NB-GA || LDH device at different scan rates ranging from 5 to 100  $\text{mV s}^{-1}$ . **c**, Long-term cycling stability of an NB-GA || LDH device at a current density of 5  $\text{A g}^{-1}$  over 5,000 consecutive GCD cycles.

Figure S19a presents typical CV curves of the NB-GA || LDH asymmetric device with various upper cutoff voltages from 1.0 to 1.7 V at a scan rate of  $10 \text{ mV s}^{-1}$ . As can be seen, the device works stably even at a high voltage of 1.7 V. However, to keep the decomposition of water to a minimum and ensure long-term stability of the device under operation, we limited the operating voltage window of the NB-GA || LDH asymmetric device to 1.5 V, which is still wider than the thermodynamic breakdown window of water and much higher than that of conventional activated carbon-based capacitors in aqueous electrolytes (0.8–1.0 V).<sup>90</sup> Figure S19b illustrates the shape retention of the CV curves at different scan rates up to  $100 \text{ mV s}^{-1}$ , demonstrating excellent rate capability and reversibility of the NB-GA || LDH asymmetric device.

The device exhibits an ultrahigh specific capacitance of  $347 \text{ F g}^{-1}$  at  $1 \text{ A g}^{-1}$ , and provides a capacitance of  $188 \text{ F g}^{-1}$  at a high specific current of  $20 \text{ A g}^{-1}$  (54% capacitance retention), indicating the excellent rate capability of the NB-GA || LDH device (Fig. 4j, main text).

In order to investigate the long-term cycling stability of the device, we performed over 5,000 GCD cycles at a specific current of  $5 \text{ A g}^{-1}$ . As shown in Figure S19c, the NB-GA || LDH device retained 81% of initial capacitance after 5,000 consecutive cycles, indicating good cycling stability.

## 18. Practical Applications



**Figure S20. Practical application of an NB-GA || MnO<sub>2</sub> prototype device.** **a**, Demonstration of the practical applicability of a single NB-GA || MnO<sub>2</sub> prototype device to a solar-powered system that makes energy on-site, and can run a clock for more than 12 min. **b**, Schematic demonstration of the circuit used for solar-powered charging of the supercapacitor.

**Table S4.** Comparison of the Electrochemical Performances of the NB-GA || NB-GA Device with Other Functionalized Graphene-Based Symmetric Devices

Symmetric device	C device at specific current	Specific energy	Cycles	Retention	Electrolyte	$\Delta V$ (V)	Ref.
Hydroquinone/graphene Hydrogels (FGHs)	441 F g <sup>-1</sup> at 1 A g <sup>-1</sup>	15.3 W h kg <sup>-1</sup>	10,000	86% at 10 A g <sup>-1</sup>	1 M H <sub>2</sub> SO <sub>4</sub>	1.0	91
Alizarin/self-assembled graphene hydrogels (AZ-SGHs)	285.6 F g <sup>-1</sup> at 1 A g <sup>-1</sup>	18.2 W h kg <sup>-1</sup> at 700 W kg <sup>-1</sup>	1,000	88% at 5 A g <sup>-1</sup>	1 M H <sub>2</sub> SO <sub>4</sub>	1.4	92
Poly(p-phenylenediamine)/graphene (PpPD/graphene)	284 F g <sup>-1</sup> at 2 A g <sup>-1</sup>	8.6 W h kg <sup>-1</sup> at 500 W kg <sup>-1</sup>	1,000	72% at 10 A g <sup>-1</sup>	1 M H <sub>2</sub> SO <sub>4</sub>	1.0	93
Nafion-functionalized reduced graphene oxide (f-RGO)	118.5 F g <sup>-1</sup> at 1 A g <sup>-1</sup>	---	1,000	no significant changes at 1 A g <sup>-1</sup>	solvent-cast Nafion	1.0	94
Acid-assisted functionalized graphene (a-FG)	417 F g <sup>-1</sup> at 50 mA g <sup>-1</sup>	14.48 W h kg <sup>-1</sup>	1,000	no significant changes at 10 A g <sup>-1</sup>	6 M KOH	1.0	95
1- Pyrene Carboxylic-Acid Functionalized Graphene	202 F g <sup>-1</sup> @ 10 mVs <sup>-1</sup>	7 W h kg <sup>-1</sup>	-	-	6 M KOH	1.0	96
Aminopyrene functionalized reduced graphene oxide (Ap-rGO)	160 F g <sup>-1</sup> @ 5 mV s <sup>-1</sup>	5.6 W h kg <sup>-1</sup>	5,000	85% at 0.5 A g <sup>-1</sup>	6 M KOH	1.0	97
Butane-1,4-diamine functionalized reduced graphene oxide (BDA-rGO)	208 F g <sup>-1</sup> at 1 A g <sup>-1</sup>	7.2 W h kg <sup>-1</sup>	10,000	92% at 1 A g <sup>-1</sup>	1 M H <sub>2</sub> SO <sub>4</sub>	1.0	98
Triethanolamine (TEA) functionalized reduced graphene oxide (TEA/rGO)	211F g <sup>-1</sup> at 1 A g <sup>-1</sup>	7.2 W h kg <sup>-1</sup>	10,000	91.7% at 2 A g <sup>-1</sup>	1 M H <sub>2</sub> SO <sub>4</sub>	1.0	99
	118 F g <sup>-1</sup> @ 10 mV s <sup>-1</sup>	25.7Wh kg <sup>-1</sup>	10,000	91.4% at 2 A g <sup>-1</sup>	1 M TEA/BF <sub>4</sub>	2.5	
p-phenylenediamine functionalized rGO(GHPPD)	303.88 F g <sup>-1</sup> at 0.5 A g <sup>-1</sup>	6.75 Wh kg <sup>-1</sup>	4,000	87.14% at 2 A g <sup>-1</sup>	2 M H <sub>2</sub> SO <sub>4</sub>	0.8	100
m-benzenediol-reduced graphene oxide hydrogels (o-rGOHG80)	221 F g <sup>-1</sup> at 1 A g <sup>-1</sup>	8.2 W h kg <sup>-1</sup> at 125 W kg <sup>-1</sup>	10,000	95.5 % at 250 mV s <sup>-1</sup>	1 M H <sub>2</sub> SO <sub>4</sub>	1.0	101
Lignosulfonate functionalized graphene hydrogels (LS-GHs)	408 F g <sup>-1</sup> at 1 A g <sup>-1</sup>	13.8 W h kg <sup>-1</sup> at 500 W kg <sup>-1</sup>	10,000	84% at 2 A g <sup>-1</sup>	PVA-H <sub>2</sub> SO <sub>4</sub> gel	1.0	102
Egg protein derived carbon/ reduced graphene oxide (EDC/rGO) composite	325 F g <sup>-1</sup> at 0.1 A g <sup>-1</sup>	11.3 W h kg <sup>-1</sup> at 25 W kg <sup>-1</sup>	10,000	~ 100% at 5 A g <sup>-1</sup>	1 M H <sub>2</sub> SO <sub>4</sub>	1.0	103
1,8-dihydroxyanthraquinone functionalized reduced graphene oxide nanosheets (DT-RGNs)	284 F g <sup>-1</sup> at 1 A g <sup>-1</sup>	12.6 W h kg <sup>-1</sup> at 700 W kg <sup>-1</sup>	10,000	92.4% at 10 A g <sup>-1</sup>	1 M H <sub>2</sub> SO <sub>4</sub>	1.1	104
Thionine functionalized 3D graphene aerogel (Th-GA)	384 F g <sup>-1</sup> at 1 A g <sup>-1</sup>	25.8 W h kg <sup>-1</sup> at 460 W kg <sup>-1</sup>	6,000	82% at 10 A g <sup>-1</sup>	1 M H <sub>2</sub> SO <sub>4</sub>	1.4	15
	235 F g <sup>-1</sup> at 1 A g <sup>-1</sup>	32.6 W h kg <sup>-1</sup> at 753.2 W kg <sup>-1</sup>	4,000	86% at 2 A g <sup>-1</sup>	1 M Na <sub>2</sub> SO <sub>4</sub>	2.0	
Nile Blue functionalized 3D graphene aerogel (NB-GA)	376 F g <sup>-1</sup> at 1 A g <sup>-1</sup>	22 W h kg <sup>-1</sup> at 426 W kg <sup>-1</sup>	6,000	91% at 5 A g <sup>-1</sup>	1 M H <sub>2</sub> SO <sub>4</sub>	1.3	<b>This work</b>

## 19. Calculations

### 19.1. Capacitance of a Single Electrode:

We calculated the capacitances of the supercapacitors based on both the CV curves and the GCD profiles. The integrated area under a CV curve is equivalent to the charge that is stored during the anodic scan and delivered during the cathodic scan. The specific capacitance can be calculated, according to the following equation:

$$C_{sp,electrode} = \frac{\int i dV}{m v \Delta V} \quad (S14)$$

where  $\int i dV$  (V.s) is the integration of the current-potential curve during the discharge,  $m$  (g) indicates the mass of the material loaded onto the electrode,  $\Delta V$  (V) is the working voltage window, and  $v$  ( $V s^{-1}$ ) is the scan rate.

We also calculated the specific capacitance from the GCD profiles based on the following equation:

$$C_{sp,electrode} = \frac{2 \times I \times \int V dt}{\Delta V^2 \times m} \quad (S15)$$

where  $\int V dt$  (V.s) is the integration of the potential-time curve during the discharge,  $m$  (g) indicates the mass of the material loaded onto the electrode,  $\Delta V$  (V) is the working voltage window and  $I$  (A) represents the discharge current.

### 19.2. Capacitance of Symmetric and Asymmetric Devices

The gravimetric (specific) capacitance of a symmetric device can be calculated from the CV curves and GCD profiles according to Equations S16 and S17 as follows:

$$C_{sp,device} = \frac{\int i dV}{m v \Delta V} \quad (S16)$$

$$C_{sp,electrode} = \frac{2 \times I \times \int V dt}{\Delta V^2 \times m} \quad (S17)$$

where  $m$  (g) indicates the total mass of the materials loaded onto both the negative and positive electrodes.

The specific capacitance of each of the positive and negative electrodes is calculated from the capacitance of a full symmetric cell according to:

$$C_{sp,electrode} (F g^{-1}) = 4 \times C_{sp,device} (F g^{-1}) \quad (S18)$$

### 19.3. Energy density and power density of symmetric and asymmetric devices

Specific energy ( $E_s$ ,  $Wh kg^{-1}$ ) and specific power ( $P_s$ ,  $W kg^{-1}$ ) are calculated based on the total mass of the materials loaded onto both the positive and negative electrodes.

$$E_{sp} = \frac{1000 \times I \times \int V dt}{3600 \times m} \quad (S19)$$

$$P_{sp} = \frac{E_{sp, device} \times 3600}{t} \quad (S20)$$

### 19.4. Mass balancing of devices

To balance the charges stored on each of the positive and negative electrodes ( $Q$ ), the mass loading ratio of the electroactive materials on each electrode is obtained by the following equation:<sup>1</sup>

$$Q_+ = Q_- \rightarrow m_+ \times \Delta V_+ \times C_+ = m_- \times \Delta V_- \times C_- \quad (S21)$$

where  $m$  is the mass of the active material (g),  $C$  is the specific capacitance ( $F g^{-1}$ ), and  $\Delta V$  is the potential range for the charge/discharge process (V). Electrochemical properties of the positive and negative electrodes are studied individually in a three-electrode cell setup. Thus, the optimal

mass ratio between the two electrodes  $m_+/m_-$  can be adjusted to get the optimal performance of an asymmetric supercapacitor.

### **19.5. Calculation of the Percentage of the Nile Blue Molecules in the NB-GA Nanocomposite**

We estimated the percentage of the Nile Blue molecules on the rGO surfaces based on the elemental analysis from the XPS experiment. Briefly, the elemental analysis shows that the wt% of N in the GA and NB-GA assemblies were 5.58% and 8.46%, respectively. Thus, 2.61% nitrogen in the NB-GA sample is related to the presence of Nile Blue in the structure. Since, there are three nitrogen atoms in the Nile Blue unit structure ( $C_{20}H_{20}N_3O$ ), the wt% of Nile Blue in the assembly is  $(3.1\% \div 14) \div 3 \times 318.41 \approx 19.8\%$ .

## REFERENCES

1. Noori, A.; El-Kady, M. F.; Rahmanifar, M. S.; Kaner, R. B.; Mousavi, M. F., Towards Establishing Standard Performance Metrics for Batteries, Supercapacitors and Beyond. *Chem. Soc. Rev.* **2019**, *48*, 1272-1341.
2. Martinez, V.; Henary, M., Nile Red and Nile Blue: Applications and Syntheses of Structural Analogues. *Chemistry* **2016**, *22*, 13764-13782.
3. Sun, Z.; Fu, H.; Deng, L.; Wang, J., Redox-Active Thionine–Graphene Oxide Hybrid Nanosheet: One-Pot, Rapid Synthesis, and Application as a Sensing Platform for Uric Acid. *Anal. Chim. Acta* **2013**, *761*, 84-91.
4. Zhou, Q.; Li, G.; Zhang, Y.; Zhu, M.; Wan, Y.; Shen, Y., Highly Selective and Sensitive Electrochemical Immunoassay of Cry1c Using Nanobody and  $\Pi$ – $\Pi$  Stacked Graphene Oxide/Thionine Assembly. *Anal. Chem.* **2016**, *88*, 9830-9836.
5. Li, B.; Zhao, J.; Onda, K.; Jordan, K. D.; Yang, J.; Petek, H., Ultrafast Interfacial Proton-Coupled Electron Transfer. *Science* **2006**, *311*, 1436-1440.
6. Chen, G.; Shi, H.; Ban, F.; Zhang, Y.; Sun, L., Determination of Trypsin Activity Using a Gold Electrode Modified with a Nanocover Composed of Graphene Oxide and Thionine. *Microchim. Acta* **2015**, *182*, 2469-2476.
7. Liu, Y.; Liu, C.-y.; Liu, Y., Investigation on Fluorescence Quenching of Dyes by Graphite Oxide and Graphene. *Appl. Surf. Sci.* **2011**, *257*, 5513-5518.
8. Loh, K. P.; Bao, Q.; Eda, G.; Chhowalla, M., Graphene Oxide as a Chemically Tunable Platform for Optical Applications. *Nat. Chem.* **2010**, *2*, 1015-1024.
9. Xu, Y.; Bai, H.; Lu, G.; Li, C.; Shi, G., Flexible Graphene Films Via the Filtration of Water-Soluble Noncovalent Functionalized Graphene Sheets. *J. Am. Chem. Soc.* **2008**, *130*, 5856-5857.
10. Krzyszkowska, E.; Walkowiak-Kulikowska, J.; Stienen, S.; Wojcik, A., Thionine–Graphene Oxide Covalent Hybrid and Its Interaction with Light. *Phys. Chem. Chem. Phys.* **2017**, *19*, 14412-14423.
11. Shervedani, R. K.; Ansarifar, E.; Foroushani, M. S., Electrocatalytic Activities of Graphene/Nile Blue Nanocomposite toward Determination of Hydrogen Peroxide and Nitrite Ion. *Electroanalysis* **2016**, *28*, 1957-1969.
12. Yan, Y.; Zhang, M.; Gong, K.; Su, L.; Guo, Z.; Mao, L., Adsorption of Methylene Blue Dye onto Carbon Nanotubes: A Route to an Electrochemically Functional Nanostructure and Its Layer-by-Layer Assembled Nanocomposite. *Chem. Mater.* **2005**, *17*, 3457-3463.
13. Zhang, D.; Fu, L.; Liao, L.; Dai, B.; Zou, R.; Zhang, C., Electrochemically Functional Graphene Nanostructure and Layer-by-Layer Nanocomposite Incorporating Adsorption of Electroactive Methylene Blue. *Electrochim. Acta* **2012**, *75*, 71-79.
14. Saleh, F. S.; Rahman, M. R.; Kitamura, F.; Okajima, T.; Mao, L.; Ohsaka, T., A Simple and Effective Way to Integrate Nile Blue Covalently onto Functionalized SWCNTs Modified GC Electrodes for Sensitive and Selective Electroanalysis of NADH. *Electroanalysis* **2011**, *23*, 409-416.
15. Shabangoli, Y.; Rahmanifar, M. S.; El-Kady, M. F.; Noori, A.; Mousavi, M. F.; Kaner, R. B., Thionine Functionalized 3D Graphene Aerogel: Combining Simplicity and Efficiency in Fabrication of a Metal-Free Redox Supercapacitor. *Adv. Energy Mater.* **2018**, 1802869.
16. Zhang, Z.; Huang, H.; Yang, X.; Zang, L., Tailoring Electronic Properties of Graphene by  $\Pi$ – $\Pi$  Stacking with Aromatic Molecules. *J. Phys. Chem. Lett.* **2011**, *2*, 2897-2905.
17. Deka, M. J.; Chowdhury, D., Tuning Electrical Properties of Graphene with Different  $\Pi$ -Stacking Organic Molecules. *J. Phys. Chem. C* **2016**, *120*, 4121-4129.
18. Rao, C. N. R.; Voggu, R., Charge-Transfer with Graphene and Nanotubes. *Mater. Today* **2010**, *13*, 34-40.
19. Mažeikienė, R.; Niaura, G.; Eicher-Lorka, O.; Malinauskas, A., Raman Spectroelectrochemical Study of Redox Dye Nile Blue Adsorbed or Electropolymerised at a Gold Electrode. *Chemija* **2019**, *30*, 78-88.
20. Poulin, P.; Jalili, R.; Neri, W.; Nallet, F.; Divoux, T.; Colin, A.; Aboutalebi, S. H.; Wallace, G.; Zakri, C., Superflexibility of Graphene Oxide. *Proc. Natl. Acad. Sci.* **2016**, *113*, 11088-11093.
21. Liu, L.; Zhang, J.; Zhao, J.; Liu, F., Mechanical Properties of Graphene Oxides. *Nanoscale* **2012**, *4*, 5910-5916.
22. Shi, R.; Han, C.; Duan, H.; Xu, L.; Zhou, D.; Li, H.; Li, J.; Kang, F.; Li, B.; Wang, G., Redox-Active Organic Sodium Anthraquinone-2-Sulfonate (AQS) Anchored on Reduced Graphene Oxide for High-Performance Supercapacitors. *Adv. Energy Mater.* **2018**, 1802088.
23. Xu, Y.; Lin, Z.; Huang, X.; Wang, Y.; Huang, Y.; Duan, X., Functionalized Graphene Hydrogel-Based High-Performance Supercapacitors. *Adv. Mater.* **2013**, *25*, 5779-5784.
24. Jana, M.; Saha, S.; Khanra, P.; Samanta, P.; Koo, H.; Murmu, N. C.; Kuila, T., Non-Covalent Functionalization of Reduced Graphene Oxide Using Sulfanilic Acid Azocromotrop and Its Application as a Supercapacitor Electrode Material. *J. Mater. Chem. A* **2015**, *3*, 7323-7331.
25. Yuan, K.; Xu, Y.; Uihlein, J.; Brunklaus, G.; Shi, L.; Heiderhoff, R.; Que, M.; Forster, M.; Chassé, T.; Pichler, T., Straightforward Generation of Pillared, Microporous Graphene Frameworks for Use in Supercapacitors. *Adv. Mater.* **2015**, *27*, 6714-6721.
26. Vishnu, N.; Kumar, A. S.; Pan, G.-T.; Yang, T. C. K., Selective Electrochemical Polymerization of 1-Naphthylamine on Carbon Electrodes and Its pH Sensing Behavior in Non-Invasive Body Fluids Useful in Clinical Applications. *Sensor Actuat. B-Chem.* **2018**, *275*, 31-42.

27. Wilson, A. J.; Molina, N. Y.; Willets, K. A., Modification of the Electrochemical Properties of Nile Blue through Covalent Attachment to Gold as Revealed by Electrochemistry and SERS. *J. Phys. Chem. C* **2016**, *120*, 21091-21098.
28. Kul, D.; Emilia Ghica, M.; Pauliukaite, R.; Brett, C. M. A., A Novel Amperometric Sensor for Ascorbic Acid Based on Poly(Nile Blue A) and Functionalised Multi-Walled Carbon Nanotube Modified Electrodes. *Talanta* **2013**, *111*, 76-84.
29. Wopschall, R. H.; Shain, I., Effects of Adsorption of Electroactive Species in Stationary Electrode Polarography. *Anal. Chem.* **1967**, *39*, 1514-1527.
30. Zhao, Y.; Wang, X.; Wang, N.; Li, M.; Li, Q.; Liu, J., Unraveling Factors Leading to High Pseudocapacitance of Redox-Active Small Aromatics on Graphene. *J. Phys. Chem. C* **2019**, *123*, 994-1002.
31. Ghosh, S.; Mathews, T.; Gupta, B.; Das, A.; Gopala Krishna, N.; Kamruddin, M., Supercapacitive Vertical Graphene Nanosheets in Aqueous Electrolytes. *Nano-Struct. Nano-Objects* **2017**, *10*, 42-50.
32. Atkins, P.; de Paula, J., *Elements of Physical Chemistry*. Oxford University Press: Oxford, 2013.
33. Weinberg, D. R.; Gagliardi, C. J.; Hull, J. F.; Murphy, C. F.; Kent, C. A.; Westlake, B. C.; Paul, A.; Ess, D. H.; McCafferty, D. G.; Meyer, T. J., Proton-Coupled Electron Transfer. *Chem. Rev.* **2012**, *112*, 4016-4093.
34. Ozdal, D.; Aydinlik, N. P.; Bodapati, J. B.; Icil, H., Self-Assembly, Optical, Thermal and Electrochemical Properties of Bis-N-Benzyl Perylene Diimide Dye. *Photochem. Photobiol. Sci.* **2017**, *16*, 262-270.
35. Skitał, P. M.; Sanecki, P. T.; Saletnik, D., Iso Points in Electrochemistry. Classification and Verification by Experiment and Theory. *Electroanalysis* **2018**, *30*, 1990-2003.
36. Kurouski, D.; Mattei, M.; Van Duyne, R. P., Probing Redox Reactions at the Nanoscale with Electrochemical Tip-Enhanced Raman Spectroscopy. *Nano Lett.* **2015**, *15*, 7956-7962.
37. Chen, X.; Wang, F.; Chen, Z., An Electropolymerized Nile Blue Sensing Film-Based Nitrite Sensor and Application in Food Analysis. *Anal. Chim. Acta* **2008**, *623*, 213-220.
38. Kul, D.; Pauliukaite, R.; Brett, C. M. A., Electrosynthesis and Characterisation of Poly(Nile Blue) Films. *J. Electroanal. Chem.* **2011**, *662*, 328-333.
39. Ni, F.; Feng, H.; Gorton, L.; Cotton, T. M., Electrochemical and SERS Studies of Chemically Modified Electrodes: Nile Blue A, a Mediator for NADH Oxidation. *Langmuir* **1990**, *6*, 66-73.
40. Madsen, J.; Canton, I.; Warren, N. J.; Themistou, E.; Blanazs, A.; Ustbas, B.; Tian, X.; Pearson, R.; Battaglia, G.; Lewis, A. L.; Armes, S. P., Nile Blue-Based Nanosized pH Sensors for Simultaneous Far-Red and Near-Infrared Live Bioimaging. *J. Am. Chem. Soc.* **2013**, *135*, 14863-70.
41. Lounasvuori, M. M.; Rosillo-Lopez, M.; Salzmann, C. G.; Caruana, D. J.; Holt, K. B., Electrochemical Characterisation of Graphene Nanoflakes with Functionalised Edges. *Faraday Discuss.* **2014**, *172*, 293-310.
42. Medina-Ramos, J.; Alligrant, T. M.; Clingenpeel, A.; Alvarez, J. C., Comparing the Hydrogen-Bonding Effect of Brønsted Bases in Solution and When They Are Covalently Bound to the Surface of Glassy Carbon Electrodes in the Electrochemical Behavior of Hydroquinone. *J. Phys. Chem. C* **2012**, *116*, 20447-20457.
43. Saraswatula, V. G.; Sharada, D.; Saha, B. K., Stronger  $\pi \cdots \pi$  Interaction Leads to a Smaller Thermal Expansion in Some Charge Transfer Complexes. *Cryst. Growth Des.* **2018**, *18*, 52-56.
44. Zhu, Z.; Jiang, H.; Guo, S.; Cheng, Q.; Hu, Y.; Li, C., Dual Tuning of Biomass-Derived Hierarchical Carbon Nanostructures for Supercapacitors: The Role of Balanced Meso/Microporosity and Graphene. *Sci. Rep.* **2015**, *5*, 15936-15936.
45. Bard, A. J.; Faulkner, L. R., *Electrochemical Methods: Fundamentals and Applications*. John Wiley and Sons: New York, USA, 2000.
46. Malinauskas, A.; Ruzgas, T.; Gorton, L., Electrochemical Study of the Redox Dyes Nile Blue and Toluidine Blue Adsorbed on Graphite and Zirconium Phosphate Modified Graphite. *J. Electroanal. Chem.* **2000**, *484*, 55-63.
47. Liu, H. H.; Lu, J. L.; Zhang, M.; Pang, D. W., Electrochemical Properties of Nile Blue Covalently Immobilized on Self-Assembled Thiol-Monolayer Modified Gold Electrodes. *Anal. Sci.* **2002**, *18*, 1339-44.
48. Wang, C.; Appleby, A. J.; Little, F. E., Criteria for Reliable Electrochemical Impedance Measurements on Li-Ion Battery Anodes. *J. Electrochem. Soc.* **2003**, *150*, A143-A148.
49. Zeng, J.; Ren, Y.; Wang, S.; Hao, Y.; Wu, H.; Zhang, S.; Xing, Y., Hierarchical Porous ZnMn<sub>2</sub>O<sub>4</sub> Microspheres Assembled by Nanosheets for High Performance Anodes of Lithium Ion Batteries. *Inorg. Chem. Front.* **2017**, *4*, 1730-1736.
50. Mei, B.-A.; Lau, J.; Lin, T.; Tolbert, S. H.; Dunn, B. S.; Pilon, L., Physical Interpretations of Electrochemical Impedance Spectroscopy of Redox Active Electrodes for Electrical Energy Storage. *J. Phys. Chem. C* **2018**, *122*, 24499-24511.
51. Thangappan, R.; Kalaiselvam, S.; Elayaperumal, A.; Jayavel, R.; Arivanandhan, M.; Karthikeyan, R.; Hayakawa, Y., Graphene Decorated with MoS<sub>2</sub> Nanosheets: A Synergetic Energy Storage Composite Electrode for Supercapacitor Applications. *Dalton Trans.* **2016**, *45*, 2637-2646.
52. Lasia, A., Modeling of Impedance of Porous Electrodes. In *Modeling and Numerical Simulations*, Schlesinger, M., Ed. Springer New York: New York, NY, 2009; pp 67-137.
53. Galal, A.; Atta, N. F.; Ali, S. M., Optimization of the Synthesis Conditions for LaNiO<sub>3</sub> Catalyst by Microwave Assisted Citrate Method for Hydrogen Production. *Appl. Catal., A* **2011**, *409-410*, 202-208.

54. Miller, J. R.; Outlaw, R.; Holloway, B., Graphene Double-Layer Capacitor with ac Line-Filtering Performance. *Science* **2010**, *329*, 1637-1639.
55. Brousse, T.; Bélanger, D.; Long, J. W., To Be or Not to Be Pseudocapacitive? *J. Electrochem. Soc.* **2015**, *162*, A5185-A5189.
56. Kim, H. S.; Cook, J. B.; Lin, H.; Ko, J. S.; Tolbert, S. H.; Ozolins, V.; Dunn, B., Oxygen Vacancies Enhance Pseudocapacitive Charge Storage Properties of MoO<sub>3-x</sub>. *Nat. Mater.* **2017**, *16*, 454-460.
57. Forghani, M.; Donne, S. W., Method Comparison for Deconvoluting Capacitive and Pseudo-Capacitive Contributions to Electrochemical Capacitor Electrode Behavior. *J. Electrochem. Soc.* **2018**, *165*, A664-A673.
58. Ardizzone, S.; Fregonara, G.; Trasatti, S., “Inner” and “Outer” Active Surface of RuO<sub>2</sub> Electrodes. *Electrochim. Acta* **1990**, *35*, 263-267.
59. Cook, J. B.; Kim, H. S.; Yan, Y.; Ko, J. S.; Robbennolt, S.; Dunn, B.; Tolbert, S. H., Mesoporous MoS<sub>2</sub> as a Transition Metal Dichalcogenide Exhibiting Pseudocapacitive Li and Na-Ion Charge Storage. *Adv. Energy Mater.* **2016**, *6*, 1501937.
60. Ma, Y.; Guo, Q.; Yang, M.; Wang, Y.; Chen, T.; Chen, Q.; Zhu, X.; Xia, Q.; Li, S.; Xia, H., Highly Doped Graphene with Multi-Dopants for High-Capacity and Ultrastable Sodium-Ion Batteries. *Energy Storage Mater.* **2018**, *13*, 134-141.
61. Jiang, Q.; Kurra, N.; Alhabeab, M.; Gogotsi, Y.; Alshareef, H. N., All Pseudocapacitive MXene-RuO<sub>2</sub> Asymmetric Supercapacitors. *Adv. Energy Mater.* **2018**, *8*, 1703043.
62. Brezesinski, T.; Wang, J.; Tolbert, S. H.; Dunn, B., Ordered Mesoporous  $\alpha$ -MoO<sub>3</sub> with Iso-Oriented Nanocrystalline Walls for Thin-Film Pseudocapacitors. *Nat. Mater.* **2010**, *9*, 146-151.
63. Kim, H.-S.; Cook, J. B.; Tolbert, S. H.; Dunn, B., The Development of Pseudocapacitive Properties in Nanosized-MoO<sub>2</sub>. *J. Electrochem. Soc.* **2015**, *162*, A5083-A5090.
64. Brezesinski, T.; Wang, J.; Senter, R.; Brezesinski, K.; Dunn, B.; Tolbert, S. H., On the Correlation between Mechanical Flexibility, Nanoscale Structure, and Charge Storage in Periodic Mesoporous CeO<sub>2</sub> Thin Films. *ACS Nano* **2010**, *4*, 967-977.
65. Kim, H.-S.; Cook, J. B.; Lin, H.; Ko, J. S.; Tolbert, S. H.; Ozolins, V.; Dunn, B., Oxygen Vacancies Enhance Pseudocapacitive Charge Storage Properties of MoO<sub>3-x</sub>. *Nat. Mater.* **2017**, *16*, 454-460.
66. Brezesinski, T.; Wang, J.; Polleux, J.; Dunn, B.; Tolbert, S. H., Templated Nanocrystal-Based Porous TiO<sub>2</sub> Films for Next-Generation Electrochemical Capacitors. *J. Am. Chem. Soc.* **2009**, *131*, 1802-1809.
67. Wang, J.; Polleux, J.; Lim, J.; Dunn, B., Pseudocapacitive Contributions to Electrochemical Energy Storage in TiO<sub>2</sub> (Anatase) Nanoparticles. *J Phys. Chem. C.* **2007**, *111*, 14925-14931.
68. Chen, Z.; Augustyn, V.; Jia, X.; Xiao, Q.; Dunn, B.; Lu, Y., High-Performance Sodium-Ion Pseudocapacitors Based on Hierarchically Porous Nanowire Composites. *ACS Nano* **2012**, *6*, 4319-4327.
69. Muller, G. A.; Cook, J. B.; Kim, H.-S.; Tolbert, S. H.; Dunn, B., High Performance Pseudocapacitor Based on 2D Layered Metal Chalcogenide Nanocrystals. *Nano Lett.* **2015**, *15*, 1911-1917.
70. Cook, J. B.; Kim, H. S.; Lin, T. C.; Lai, C. H.; Dunn, B.; Tolbert, S. H., Pseudocapacitive Charge Storage in Thick Composite MoS<sub>2</sub> Nanocrystal-Based Electrodes. *Adv. Energy Mater.* **2017**, *7*, 1601283.
71. Chao, D.; Zhu, C.; Yang, P.; Xia, X.; Liu, J.; Wang, J.; Fan, X.; Savilov, S. V.; Lin, J.; Fan, H. J., Array of Nanosheets Render Ultrafast and High-Capacity Na-Ion Storage by Tunable Pseudocapacitance. *Nat. Commun.* **2016**, *7*, 12122.
72. Jia, G.; Chao, D.; Tiep, N. H.; Zhang, Z.; Fan, H. J., Intercalation Na-Ion Storage in Two-Dimensional MoS<sub>2-x</sub>Se<sub>x</sub> and Capacity Enhancement by Selenium Substitution. *Energy Storage Mater.* **2018**, *14*, 136-142.
73. Xie, F.; Zhang, L.; Su, D.; Jaroniec, M.; Qiao, S. Z., Na<sub>2</sub>Ti<sub>3</sub>O<sub>7</sub>@ N-Doped Carbon Hollow Spheres for Sodium-Ion Batteries with Excellent Rate Performance. *Adv. Mater.* **2017**, *29*, 1601283.
74. Zhang, L.; Zhao, K.; Yu, R.; Yan, M.; Xu, W.; Dong, Y.; Ren, W.; Xu, X.; Tang, C.; Mai, L., Phosphorus Enhanced Intermolecular Interactions of SnO<sub>2</sub> and Graphene as an Ultrastable Lithium Battery Anode. *Small* **2017**, *13*, 1603973.
75. Tang, J.; Ni, S.; Chao, D.; Liu, J.; Yang, X.; Zhao, J., High-Rate and Ultra-Stable Na-Ion Storage for Ni<sub>3</sub>S<sub>2</sub> Nanoarrays Via Self-Adaptive Pseudocapacitance. *Electrochim. Acta* **2018**, *265*, 709-716.
76. Guan, C.; Chao, D.; Wang, Y.; Wang, J.; Liu, J., Confined Fe<sub>2</sub>O<sub>3</sub> Nanoparticles on Graphite Foam as High-Rate and Stable Lithium-Ion Battery Anode. *Part. Part. Syst. Char.* **2016**, *33*, 487-492.
77. Navarro-Suárez, A. M.; Casado, N.; Carretero-González, J.; Mecerreyes, D.; Rojo, T., Full-Cell Quinone/Hydroquinone Supercapacitors Based on Partially Reduced Graphite Oxide and Lignin/PEDOT Electrodes. *J Mater. Chem. A.* **2017**, *5*, 7137-7143.
78. Li, D.; Zhang, L.; Chen, H.; Wang, J.; Ding, L.-X.; Wang, S.; Ashman, P. J.; Wang, H., Graphene-Based Nitrogen-Doped Carbon Sandwich Nanosheets: A New Capacitive Process Controlled Anode Material for High-Performance Sodium-Ion Batteries. *J Mater. Chem. A.* **2016**, *4*, 8630-8635.
79. Qiu, M.; Sun, P.; Shen, L.; Wang, K.; Song, S.; Yu, X.; Tan, S.; Zhao, C.; Mai, W., WO<sub>3</sub> Nanoflowers with Excellent Pseudo-Capacitive Performance and the Capacitance Contribution Analysis. *J Mater. Chem. A.* **2016**, *4*, 7266-7273.

80. Zhi, J.; Reiser, O.; Wang, Y.; Hu, A., A High Performance Flexible All Solid State Supercapacitor Based on the MnO<sub>2</sub> Sphere Coated Macro/Mesoporous Ni/C Electrode and Ionic Conducting Electrolyte. *Nanoscale* **2016**, *8*, 11976-11983.
81. Wu, L.; Lang, J.; Zhang, P.; Zhang, X.; Guo, R.; Yan, X., Mesoporous Ni-Doped MnCo<sub>2</sub>O<sub>4</sub> Hollow Nanotubes as an Anode Material for Sodium Ion Batteries with Ultralong Life and Pseudocapacitive Mechanism. *J Mater. Chem. A* **2016**, *4*, 18392-18400.
82. Hu, X.; Li, C.; Lou, X.; Yang, Q.; Hu, B., Hierarchical CuO Octahedra Inherited from Copper Metal–Organic Frameworks: High-Rate and High-Capacity Lithium-Ion Storage Materials Stimulated by Pseudocapacitance. *J Mater. Chem. A* **2017**, *5*, 12828-12837.
83. Wei, Q.; Liu, J.; Feng, W.; Sheng, J.; Tian, X.; He, L.; An, Q.; Mai, L., Hydrated Vanadium Pentoxide with Superior Sodium Storage Capacity. *J Mater. Chem. A* **2015**, *3*, 8070-8075.
84. Zhao, C.; Yu, C.; Zhang, M.; Huang, H.; Li, S.; Han, X.; Liu, Z.; Yang, J.; Xiao, W.; Liang, J., Ultrafine MoO<sub>2</sub>-Carbon Microstructures Enable Ultralong-Life Power-Type Sodium Ion Storage by Enhanced Pseudocapacitance. *Adv. Energy Mater.* **2017**, *7*, 1602880.
85. Jian, Z.; Raju, V.; Li, Z.; Xing, Z.; Hu, Y. S.; Ji, X., A High-Power Symmetric Na-Ion Pseudocapacitor. *Adv. Funct. Mater.* **2015**, *25*, 5778-5785.
86. Tao, Q.; Dahlqvist, M.; Lu, J.; Kota, S.; Meshkian, R.; Halim, J.; Palisaitis, J.; Hultman, L.; Barsoum, M. W.; Persson, P. O. Å.; Rosen, J., Two-Dimensional Mo<sub>1.33</sub>C MXene with Divacancy Ordering Prepared from Parent 3D Laminate with in-Plane Chemical Ordering. *Nat. Commun.* **2017**, *8*, 14949.
87. Javed, M. S.; Han, X.; Hu, C.; Zhou, M.; Huang, Z.; Tang, X.; Gu, X., Tracking Pseudocapacitive Contribution to Superior Energy Storage of MnS Nanoparticles Grown on Carbon Textile. *ACS Appl. Mater. Interfaces* **2016**, *8*, 24621-24628.
88. Ajay, A.; Paravannoor, A.; Joseph, J.; Amruthalakshmi, V.; Anoop, S.; Nair, S. V.; Balakrishnan, A., 2D Amorphous Frameworks of NiMoO<sub>4</sub> for Supercapacitors: Defining the Role of Surface and Bulk Controlled Diffusion Processes. *Appl. Surf. Sci.* **2015**, *326*, 39-47.
89. Shao, Y.; El-Kady, M. F.; Sun, J.; Li, Y.; Zhang, Q.; Zhu, M.; Wang, H.; Dunn, B.; Kaner, R. B., Design and Mechanisms of Asymmetric Supercapacitors. *Chem. Rev.* **2018**, *118*, 9233-9280.
90. Zhou, C.; Zhang, Y.; Li, Y.; Liu, J., Construction of High-Capacitance 3D CoO@Polypyrrole Nanowire Array Electrode for Aqueous Asymmetric Supercapacitor. *Nano Lett.* **2013**, *13*, 2078-2085.
91. Xu, Y.; Lin, Z.; Huang, X.; Wang, Y.; Huang, Y.; Duan, X., Functionalized Graphene Hydrogel-Based High-Performance Supercapacitors. *Adv. Mater.* **2013**, *25*, 5779-5784.
92. An, N.; An, Y.; Hu, Z.; Guo, B.; Yang, Y.; Lei, Z., Graphene Hydrogels Non-Covalently Functionalized with Alizarin: An Ideal Electrode Material for Symmetric Supercapacitors. *J. Mater. Chem. A* **2015**, *3*, 22239-22246.
93. Jaidev; Ramaprabhu, S., Poly(*P*-Phenylenediamine)/Graphene Nanocomposites for Supercapacitor Applications. *J. Mater. Chem.* **2012**, *22*, 18775-18783.
94. Choi, B. G.; Hong, J.; Hong, W. H.; Hammond, P. T.; Park, H., Facilitated Ion Transport in All-Solid-State Flexible Supercapacitors. *ACS Nano* **2011**, *5*, 7205-7213.
95. Fang, Y.; Luo, B.; Jia, Y.; Li, X.; Wang, B.; Song, Q.; Kang, F.; Zhi, L., Renewing Functionalized Graphene as Electrodes for High-Performance Supercapacitors. *Adv. Mater.* **2012**, *24*, 6348-6355.
96. Ghosh, S.; An, X.; Shah, R.; Rawat, D.; Dave, B.; Kar, S.; Talapatra, S., Effect of 1- Pyrene Carboxylic-Acid Functionalization of Graphene on Its Capacitive Energy Storage. *J. Phys. Chem. C* **2012**, *116*, 20688-20693.
97. Teo, E. Y. L.; Lim, H. N.; Jose, R.; Chong, K. F., Aminopyrene Functionalized Reduced Graphene Oxide as a Supercapacitor Electrode. *RSC Adv.* **2015**, *5*, 38111-38116.
98. Song, B.; Zhao, J.; Wang, M.; Mullavey, J.; Zhu, Y.; Geng, Z.; Chen, D.; Ding, Y.; Moon, K.-s.; Liu, M., Systematic Study on Structural and Electronic Properties of Diamine/Triamine Functionalized Graphene Networks for Supercapacitor Application. *Nano Energy* **2017**, *31*, 183-193.
99. Song, B.; Sizemore, C.; Li, L.; Huang, X.; Lin, Z.; Moon, K.-s.; Wong, C.-P., Triethanolamine Functionalized Graphene-Based Composites for High Performance Supercapacitors. *J. Mater. Chem. A* **2015**, *3*, 21789-21796.
100. Lu, X.; Li, L.; Song, B.; Moon, K.-s.; Hu, N.; Liao, G.; Shi, T.; Wong, C., Mechanistic Investigation of the Graphene Functionalization Using *P*-Phenylenediamine and Its Application for Supercapacitors. *Nano Energy* **2015**, *17*, 160-170.
101. Liu, C.; Han, G.; Chang, Y.; Xiao, Y.; Zhou, H.; Shi, G., High-Performance Supercapacitors Based on the Reduced Graphene Oxide Hydrogels Modified by Trace Amounts of Benzenediols. *Chem. Eng. J.* **2017**, *328*, 25-34.
102. Hwang, J. Y.; El-Kady, M. F.; Li, M.; Lin, C.-W.; Kowal, M.; Han, X.; Kaner, R. B., Boosting the Capacitance and Voltage of Aqueous Supercapacitors Via Redox Charge Contribution from Both Electrode and Electrolyte. *Nano Today* **2017**, *15*, 15-25.
103. Ma, H.; Li, C.; Zhang, M.; Hong, J.-D.; Shi, G., Graphene Oxide Induced Hydrothermal Carbonization of Egg Proteins for High-Performance Supercapacitors. *J. Mater. Chem. A* **2017**, *5*, 17040-17047.
104. An, N.; Hu, Z.; Wu, H.; Yang, Y.; Lei, Z.; Dong, W., Organic Multi-Electron Redox Couple-Induced Functionalization for Enabling Ultrahigh Rate and Cycling Performances of Supercapacitors. *J. Mater. Chem. A* **2017**, *5*, 25420-25430.